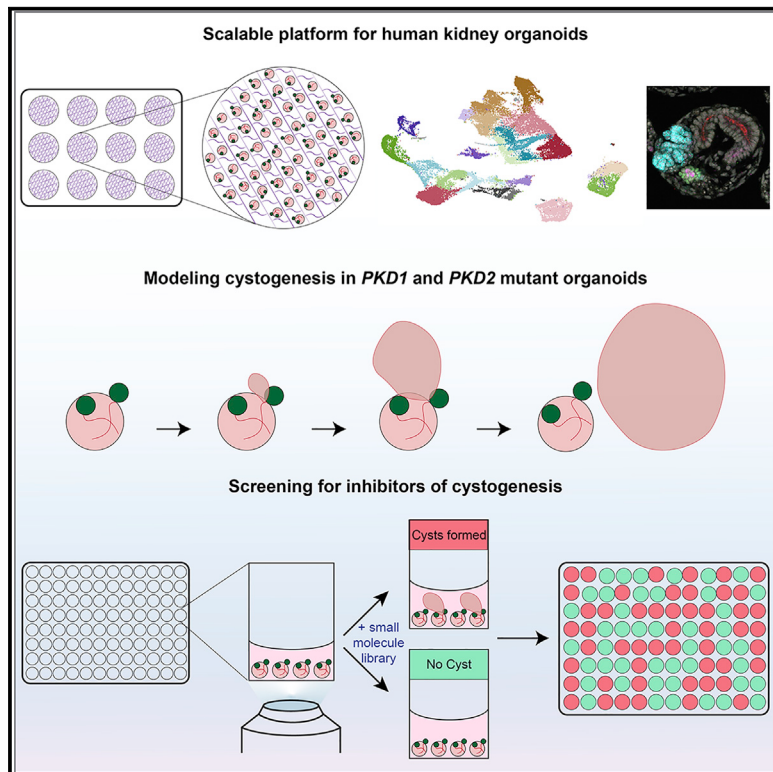


## A scalable organoid model of human autosomal dominant polycystic kidney disease for disease mechanism and drug discovery

### Graphical abstract



### Authors

Tracy Tran, Cheng Jack Song,  
Trang Nguyen, ..., Nils O. Lindström,  
Daniel C.-H. Lin, Andrew P. McMahon

### Correspondence

amcmahon@med.usc.edu

### In brief

We describe a scalable platform to efficiently generate thousands of comparable human kidney organoids. In this, *PKD1* and *PKD2* mutant organoids displayed robust cystogenesis. We generated a small-molecule screening workflow that identified compounds inhibiting cyst formation and later growth. The platform will facilitate kidney disease modeling and high-throughput drug screens.

### Highlights

- Scalable human kidney organoid platform with 1–2 nephron-like structures/organoid
- Comparative scRNA-seq profiling of *in vivo* and *in vitro* kidney programs
- *PKD1* and *PKD2* mutant kidney organoids display efficient cyst formation
- Identification of cyst-inhibitory compounds from small-molecule screens



## Article

# A scalable organoid model of human autosomal dominant polycystic kidney disease for disease mechanism and drug discovery

Tracy Tran,<sup>1,3,6</sup> Cheng Jack Song,<sup>1,2,6</sup> Trang Nguyen,<sup>1</sup> Shun-Yang Cheng,<sup>1</sup> Jill A. McMahon,<sup>1</sup> Rui Yang,<sup>1</sup> Qiuyu Guo,<sup>1,4</sup> Balint Der,<sup>1</sup> Nils O. Lindström,<sup>1</sup> Daniel C.-H. Lin,<sup>2,5</sup> and Andrew P. McMahon<sup>1,7,\*</sup>

<sup>1</sup>Department of Stem Cell Biology and Regenerative Medicine, Broad-CIRM Center, Keck School of Medicine, University of Southern California, Los Angeles, CA 90089, USA

<sup>2</sup>Amgen Research, Cardiometabolic Disorders, 1120 Veterans Blvd, South San Francisco, CA 94080, USA

<sup>3</sup>Present address: Department of Biological Chemistry, David Geffen School of Medicine, University of California, Los Angeles, Los Angeles, CA 90095, USA

<sup>4</sup>Present address: Department of Neurology, David Geffen School of Medicine, University of California, Los Angeles, Los Angeles, CA 90095, USA

<sup>5</sup>Present address: 23andMe, 349 Oyster Point Blvd, South San Francisco, CA 94080, USA

<sup>6</sup>These authors contributed equally

<sup>7</sup>Lead contact

\*Correspondence: amcmahon@med.usc.edu

<https://doi.org/10.1016/j.stem.2022.06.005>

## SUMMARY

Human pluripotent stem-cell-derived organoids are models for human development and disease. We report a modified human kidney organoid system that generates thousands of similar organoids, each consisting of 1–2 nephron-like structures. Single-cell transcriptomic profiling and immunofluorescence validation highlighted patterned nephron-like structures utilizing similar pathways, with distinct morphogenesis, to human nephrogenesis. To examine this platform for therapeutic screening, the polycystic kidney disease genes *PKD1* and *PKD2* were inactivated by gene editing. *PKD1* and *PKD2* mutant models exhibited efficient and reproducible cyst formation. Cystic outgrowths could be propagated for months to centimeter-sized cysts. To shed new light on cystogenesis, 247 protein kinase inhibitors (PKIs) were screened in a live imaging assay identifying compounds blocking cyst formation but not overall organoid growth. Scaling and further development of the organoid platform will enable a broader capability for kidney disease modeling and high-throughput drug screens.

## INTRODUCTION

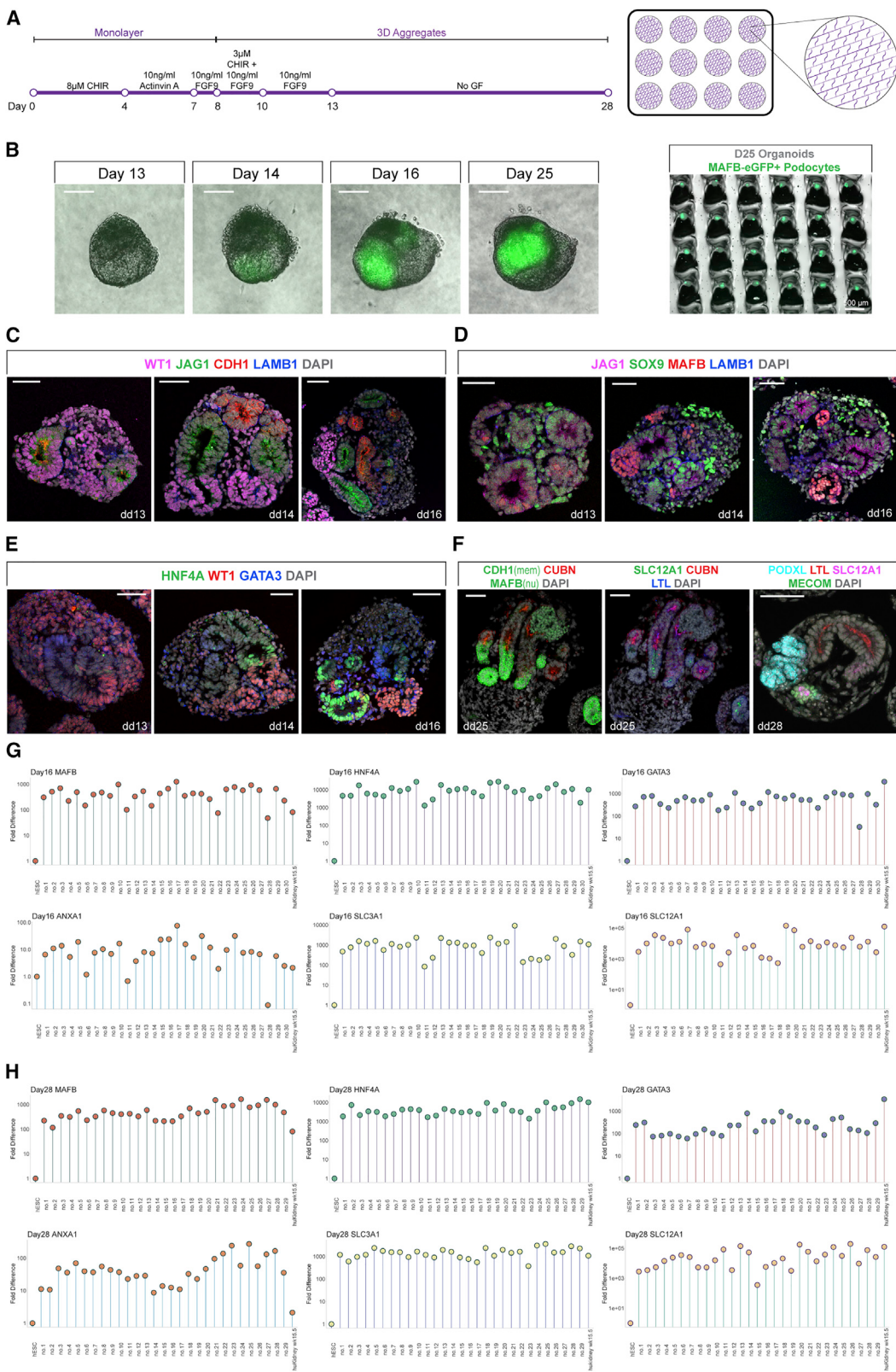
The human kidney performs the vital task of filtering blood through a network of around a million nephrons, maintaining the homeostasis of tissue fluid (Nyengaard and Bendtsen, 1992; Sasaki et al., 2019). Hormonal interactions also regulate hematopoiesis, blood pressure, and bone composition. As a consequence, the loss of renal activity in chronic disease results in secondary complications, including anemia, increased cardiovascular risk, bone disorders, and nutritional problems (Thomas et al., 2008). Chronic kidney disease affects up to 15% of the adult population in the United States (Johansen et al., 2021). Treatment options remain largely limited to dialysis and kidney transplantation, casting a burden on the healthcare system. Improving approaches to better understand and model human kidney disease is an important priority.

Multiple research groups have pioneered the generation of kidney organoid systems (Czerniecki et al., 2018; Freedman et al., 2015; Kumar et al., 2019; Lam et al., 2014; Low et al.,

2019; Morizane et al., 2015; Taguchi and Nishinakamura, 2017; Taguchi et al., 2014; Takasato et al., 2014, 2015). In these model systems, human pluripotent stem cells (PSCs) differentiate into organized 3D structures comprising multiple kidney cell types of the nephron lineage and potentially the ureteric epithelial collecting system lineage (Howden et al., 2019; Taguchi and Nishinakamura, 2017; Uchimura et al., 2020; Howden et al., 2021). Kidney organoids have been used to explore developmental processes (Czerniecki et al., 2018; Low et al., 2019; Przepiorksi et al., 2018; Taguchi et al., 2014), examine physiological activities (van den Berg et al., 2018; Kumar et al., 2019; Low et al., 2019), model disease (Forbes et al., 2018; Freedman et al., 2015; Hale et al., 2018; Kim et al., 2017; Low et al., 2019), and identify disease modulators (Czerniecki et al., 2018). Grafted organoids have been reported to generate a renal filtrate (van den Berg et al., 2018; Low et al., 2019; Xinaris et al., 2012).

Despite the burden of kidney disease, only modest progress has been made in identifying effective drugs. Autosomal dominant polycystic kidney disease (ADPKD), with ~93% of the





(legend on next page)

cases attributed to mutations in the *PKD1* or *PKD2* gene, is the most common monogenic cause of end-stage kidney disease and among the most common autosomal dominant gene mutations in the human population (Harris and Torres, 2018). Until recently, there has been no pharmacological intervention to help ADPKD disease patients. In 2018, the US Food and Drug Administration approved tolvaptan, an AVPR2 inhibitory drug that slowed disease progression in a subset of ADPKD patients (Beaudoin et al., 2019; Higashihara et al., 2011; Hopp et al., 2015; Reif et al., 2011; Torres et al., 2016, 2017). AVPR2 is restricted to a subset of principal cell and principal-cell-like epithelial cell types in the connecting region of the nephron and collecting system (Ransick et al., 2019; Kidney Cell Explorer). Broader-acting drugs are needed to target both cyst initiation and cystic growth throughout the nephron and collecting system.

Several groups have reported cystic growth in PKD1 and PKD2 mutant kidney organoid cultures where rare cystic outgrowths are augmented by forskolin, consistent with cyclic AMP (cAMP) levels driving cystogenesis (Cruz et al., 2017; Czerniecki et al., 2018; Freedman et al., 2015; Kuraoka et al., 2020). Others have failed to observe cyst formation *in vitro* in a different organoid model system (Kumar et al., 2019). To date, screens have been low throughput, relying on manually displacing organoids from a retaining extracellular gel and focused on identifying small molecules enhancing cyst formation (Czerniecki et al., 2018). Although cyst-suppressing screens using mouse 3D cysts have been reported (Asawa et al., 2020; Booij et al., 2017; Booij et al., 2020; Chang et al., 2018), there are no reports of human organoid-based screens that could potentially identify therapeutic small-molecule candidates for ADPKD.

Cost, scalability, and reproducibility are further challenges to the wider adoption of kidney organoid models. Here, we developed, characterized, and validated a simple and readily scalable, cost-effective kidney organoid platform for modeling ADPKD, identifying novel compounds blocking cyst initiation and inhibiting cyst expansion in both PKD1 and PKD2 mutant models.

## RESULTS

### A scalable platform for generating human kidney organoids with nephron-like structures

To achieve a reproducible, large-scale production of 3D kidney organoids, we utilized commercially available EZSPHERE 12-well plates, which are constructed using laser-based micro-fabrication to contain uniform microwells of 800- $\mu\text{m}$  diameter and 400- $\mu\text{m}$  depth (Sato et al., 2016). As each well contains 420 microwells, a single plate can generate over 5,000 organoids. At differentiation day 8 (dd8), cells were dissociated into single cells, and 600,000 cells were reseeded in each well of the

EZSPHERE plate to produce about 400 3D aggregates comprising approximately 1,500 cells per aggregate in each well (Figure 1A). We used a validated MAFB-P2A-eGFP H9 hESC line (Tran et al., 2019) to visualize the formation of podocyte-like cells in the organoids and observed the emergence of eGFP+ cells at day 14 of differentiation (Figure 1B), a similar timing to published kidney organoid platforms which typically use many more cells (100,000 or greater) to seed organoid formation in 96-well plates (Tran et al., 2019). At dd25, each organoid in the EZSPHERE platform had 1 or 2 eGFP+ clusters, reflecting the formation of 1–2 nephron-like structures per organoid (Figure 1B).

A number of recent studies have provided insight into human nephrogenesis (Cao et al., 2020; Hochane et al., 2019; Kim et al., 2019; Lindström et al., 2018a, 2018b, 2018c, 2018d; Menon et al., 2018; Tran et al., 2019), identifying stage-specific regional markers (Figure S1A) that can be applied to the characterization of organoid development. Immuno-analysis (Figures 1C–1F and S1B–S1D) and transcriptional profiling using quantitative polymerase chain reaction (qPCR; Figure S1E) highlighted the robust upregulation of nephrogenic signatures (including *WT1*, *PAX2*, *MAFB*, *HNF4A*, *GATA3*, *SLC3A1*, and *SLC12A1*) over the differentiation time course.

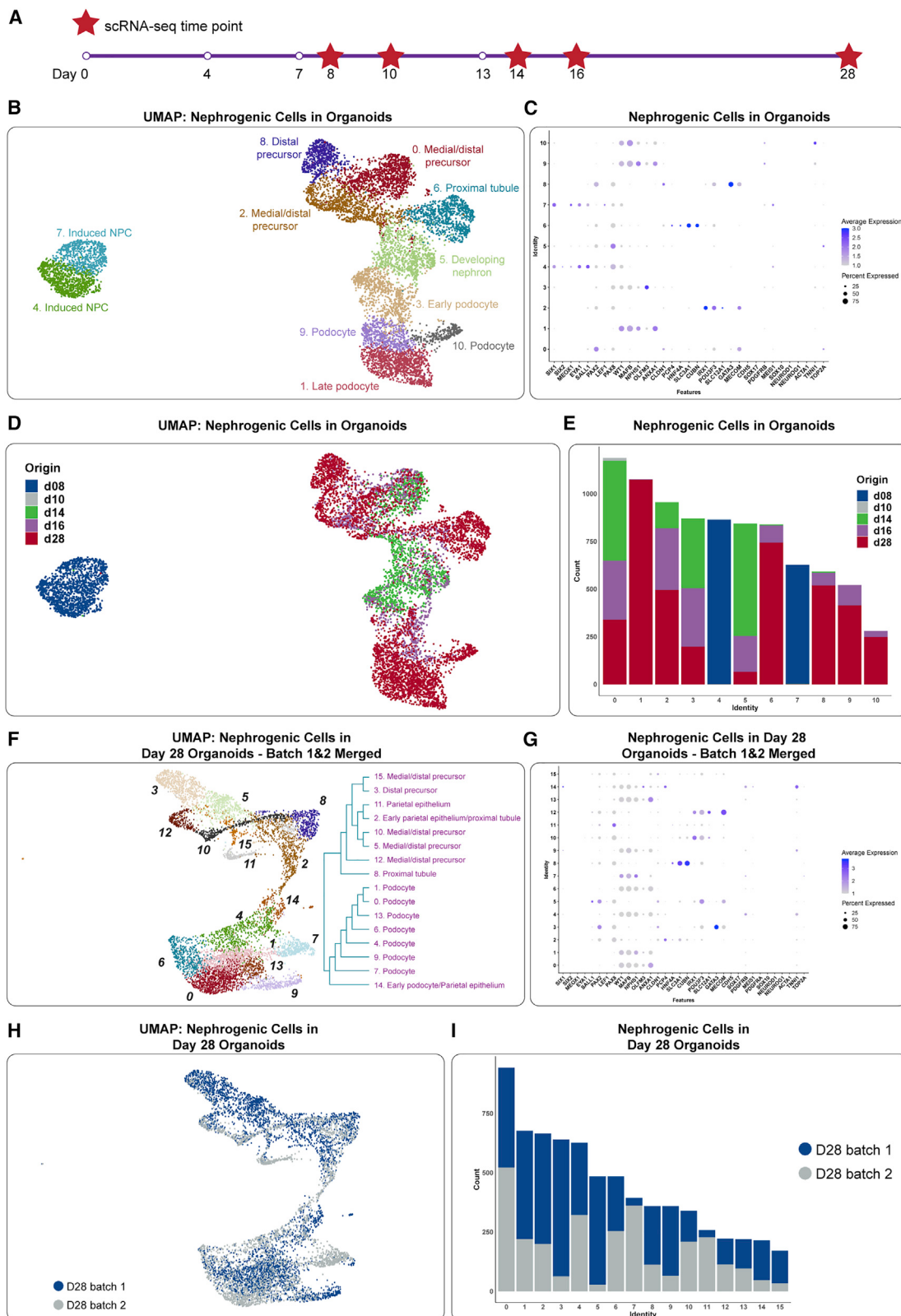
On dd13, we documented the presence of CDH1+ epithelial structures with WT1-high and WT1-low domains, reminiscent of polarization in the early renal vesicle *in vivo* (Figure 1C; Figure S1A). This time point also marked the emergence of cells with signatures of proximal nephron segment precursors (MAFB+ or WT1+), medial precursors (MAFB-/SOX9-/JAG1+ or HNF4A+), and distal nephron precursors (SOX9+ or GATA3+) (Figures 1C–1E; Figures S1A and S1B). At dd14 and dd16, the segmentation of developing nephron-like structures was more apparent with serially ordered proximal, medial, and distal precursor domains (Figures 1C–1E; Figure S1A). In dd25 organoids, we also detected the presence of WT1+ HNF4A+, HNF4A+POU3F3+, and GATA3+POU3F3+ nephron subdomains (Figure S1D). Though these segments have not been fate mapped in the mammalian kidney, HNF4A+ cells are predicted to give rise to proximal tubule segments, consistent with genetic studies in the mouse (Marable et al., 2018), and GATA3+ cells to distal nephron structures (Lindström et al., 2021). The expression of genes associated with segmental functions was also detected at dd25: MAFB+ podocyte-like cell clusters were adjacent to a CUBN+ proximal tubule-like segment, which connected with an SLC12A1+ ascending LoH-like segment (Figures 1F and S1C).

A more extensive immunofluorescence analysis comparing dd13, 14, 22, and 28 highlighted epithelial structures with the concerted emergence of distinct regional domains of the transcriptional regulators MAFB and SOX9 in PAX2+ nephron-like

**Figure 1. A scalable platform for human kidney organoid production**

- (A) Schematic diagram of directed differentiation to generate kidney organoids.
- (B) Brightfield (gray scale) and fluorescent (green) images of kidney organoids derived from MAFB-P2A-eGFP H9 hESC. Scale bars indicate 50  $\mu\text{m}$  unless labeled differently.
- (C–F) Immunofluorescent analyses of MAFB-P2A-eGFP organoids at various differentiation time points. Scale bars indicate 50  $\mu\text{m}$ .
- (G and H) qPCR analyses of *MAFB*, *SLC3A1*, *SLC12A1*, and *GATA3* expression in individual organoids from 2 batches of differentiation (batch 1: no. 1–10; batch 2: no. 11–20) at dd16 (G) and dd28 (H).

See also Figure S1.

**Figure 2. Single-cell transcriptomic profiling of kidney organoids**

(A) Schematic diagram describing scRNA-seq time points.

(B) UMAP reduction of nephrogenic cell clusters in kidney organoids, colored by clusters.

(legend continued on next page)

tubules progressing to PODXL+ podocytes connected to an LTL+ proximal tubule region, followed by an SLC12A1+ distal segment and terminal MECOM+ domain (Figures S1B and S1C). In summary, although the kidney organoids collectively lacked the stereotypical morphogenesis reported for mouse and human nephrogenesis (Lindström et al., 2021), polarization and patterning generated segmented early nephron-like structures with reasonable uniformity in the kidney organoids. Further, consistent with all published studies to date, we only observed weak expression of the distal convoluted tubule gene *SLC12A3* (Figure S1E): *SLC12A3* could not be detected by immunofluorescence. Further optimization is needed to improve distal patterning outcomes.

To assess the uniformity of development in individual organoids, qPCR was performed on 30 individual organoids at dd16 and dd28, sampling three independent batches of differentiation (10 individual organoids/batch). Each organoid showed a strong transcriptional signature for nephron segmentation, including *MAFB*, *HNF4A*, *GATA3*, *ANXA1*, *SLC3A1*, and *SLC12A1* (Figures 1G, 1H, and S1F). Whereas *MAFB* levels were relatively stable to the last stage of culture, there is a trend in the downregulation of the expression of early nephron transcription factor (TF) genes, *HNF4A* and *GATA3*, although mature nephron signature genes *ANXA1*, *SLC3A1*, and *SLC12A1* were upregulated in dd28 organoids (Figure S1F).

To demonstrate the reproducibility of the cell culture model, organoids were generated from the KOLF2.1J human induced PSC (iPSC) line (Skarnes et al., 2021), adjusting the CHIR99021 level to 7 µM during the initial 4 days of differentiation (detailed in STAR Methods). Transcriptional profiling using qPCR highlighted the formation of nephron progenitor cells (NPCs) at dd8 (*SIX1*, *SIX2*, *PAX2*, and *WT1*), early patterned nephron structures at dd16 (*PAX2*, *WT1*, *GATA3*, and *MAFB*), and the expression of mature regional cell markers at dd28 (*MAFB*, *SLC3A1*, *SLC12A1*, and *SLC12A3*) (Figures S1H and S1I). Immunofluorescent analyses validated the formation of early nephron-like segments at dd16 and more mature nephron fates at dd28 (Figure S1G).

### Developmental trajectories of nephron-like cell types

To further examine the emergence of nephron-like cells in these organoids, we applied single-cell RNA sequencing (scRNA-seq) technology to capture single-cell transcriptomic profiles at dd8, dd10, dd14, dd16, and dd28 (Figures 2A and S2A–S2D). After filtering low-quality cells and clustering in Seurat version 3, cluster identities were assigned through the expression of well-established cell markers (Figures S2A and S2B; Table S1). Nephrogenic signatures were identified in clusters 2, 4, 5, 6, 7, 11, 12, 19, and 22. In addition, and in agreement with single-cell analysis

from several groups of organoids founded on aggregation of much larger numbers of NPCs (Combes et al., 2019; Kumar et al., 2019; Tran et al., 2019; Wu et al., 2018), we observed a variety of non-nephron cell types, including: interstitial cells expressing *PDGFRB* (clusters 0 and 18), *SOX17*+ *CDH5*+ endothelial cells (cluster 24), *NEUROD1* and *NEUROG1* expressing neuron-like cells (clusters 8, 14, and 16), *SOX10*+ neural crest-like cells (clusters 1, 10, and 15), *TNNI1*+ *ACTC1*+ muscle-like cells (cluster 23), as well as developing neuron-like cells (clusters 13, 20, and 21, as identified by gene ontology (GO) terms analysis) (Figures S2A and S2B; Table S1).

To interrogate the developmental trajectory of the nephrogenic lineage in our culture model, we subset cells annotated to nephron-related cell types and re-clustered these cells to refine the analysis and to remove proliferating cells and additional non-nephrogenic cell types. The final nephrogenic lineage extraction contained 8,654 cells from 4 time points: days 8, 14, 16, and 28 (Figures 2B–2E). Re-clustering identified cells with strong transcriptional characteristics of induced nephron progenitors, early and late podocytes, medial and distal precursors, and proximal tubule cells (Figures 2B and 2C). When examining the origins contributing to the various nephrogenic identities, we noticed that induced nephron progenitor-like clusters (clusters 4 and 7) were predominantly represented in the day-8 samples, as expected, while day-10, -14, and -16 cells highlighted nephron segment precursors. Late podocyte-like cells and proximal tubule-like cells were detected in day-8 organoids, and medial/distal precursor cells were also observed in organoids of this late time point (Figures 2D and 2E).

Consistent with a nephron segmental patterning, organoid nephrogenic lineage cells expressed TF genes shown to be essential for mouse nephron segmentation and also known to be present in early nephron structures in the human kidney (Lindström et al., 2018c, 2018d): *EYA1*, *MEOX1*, and *SIX1* (Xu et al., 1999, 2003), *SIX2* (Kobayashi et al., 2008; Self et al., 2006), *SALL1* (Basta et al., 2014), *HNF4A* (Marable et al., 2018), *WT1* (Berry et al., 2015; Guo et al., 2004; Hartwig et al., 2010; Kann et al., 2015), *PAX2* and *PAX8* (Grote et al., 2006; Naiman et al., 2017), *MAFB* (Moriguchi et al., 2006; Sadl et al., 2002), *FOXC1* (Kume et al., 2000; Motojima et al., 2017), *LHX1* (Cirio et al., 2011; Kobayashi et al., 2005), *LEF1*, which is an effector of the canonical Wnt pathway (Park et al., 2012), *HNF1B* (Heliot et al., 2013; Naylor et al., 2013), *POU3F3* (Nakai et al., 2003), and *SOX9* (important for ureteric branching and present in the distal nephron, but its role in nephron patterning has not been explored) (Reginensi et al., 2011). Thus, it is likely that core nephrogenic programs were activated in the *in vitro* system and underlie the specification and patterning of nephron-like cell types (Figure S2E).

(C) Dot plot of marker genes used for identification of nephrogenic cell clusters in organoids.

(D) UMAP reduction of nephrogenic cells in kidney organoids, colored by their origins.

(E) Bar graph of cell count presenting contribution of different original identities to various clusters of the nephrogenic cells in kidney organoids.

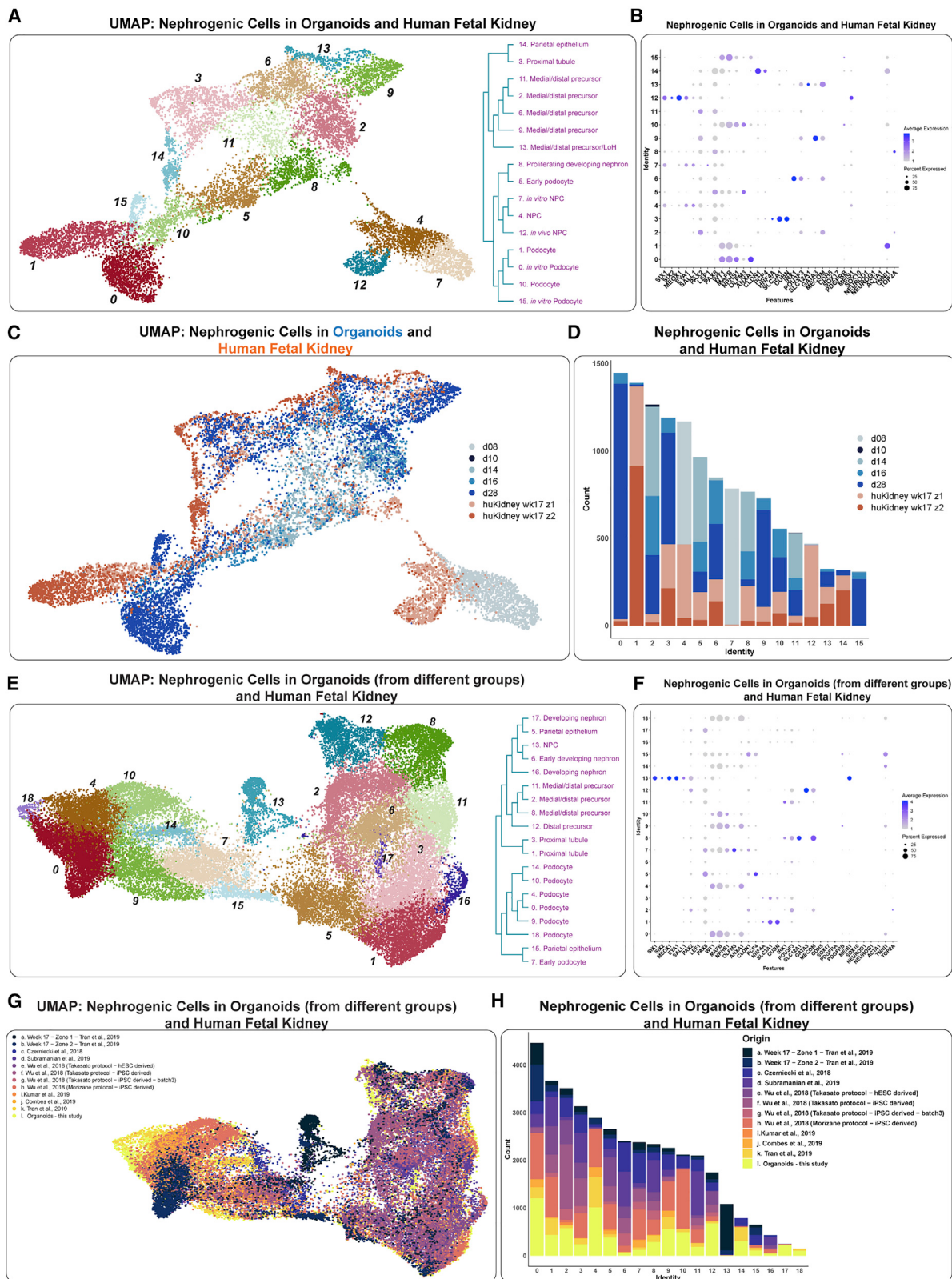
(F) UMAP reduction of integrated dd28 nephrogenic cells from two independent batches of kidney organoid differentiation, colored by clusters, and hierarchical clustering of cell identities.

(G) Dot plot of gene markers used for identification of integrated dd28 nephrogenic cells from two independent batches of kidney organoid differentiation.

(H) UMAP reduction of integrated dd28 nephrogenic cells from two independent batches of differentiation, colored by their origins.

(I) Bar graph of cell count presenting the contribution of different original identities to various clusters of the integrated dd28 nephrogenic cells from two independent batches of differentiation.

See also Figure S2 and Table S1.



(legend on next page)

To assess the reproducibility of organoid differentiation outcomes in our model system, we used scRNA-seq to compare two independent batches at dd28: 14,193 cells from batch 1 and 7,388 cells from batch 2 (Figures S2F–S2I). Nephrogenic (clusters 0, 1, 3, 8, 9, 14, 16, 19, 25, and 27), interstitial (clusters 2 and 20), and non-kidney lineages (clusters 4, 5, 6, 7, 10, 12, 13, 15, 17, 18, 21, 22, 23, and 26) showed broad representation in both batches (Figures S2F–S2I), though batch 1 dominated the composition of clusters 17 and 18 (neural crest-like cells), 24 (muscle-like cells), 25 (podocytes), and 26 (developing neuron-like cells), suggesting some quantitative variability from batch to batch. Cells of the nephrogenic lineage (7,055 cells) were re-clustered and clusters identified based on marker gene expression (Figures 2F–2I). Both batches showed overlapping segment-specific representation in podocytes (clusters 0, 1, 4, 6, 7, 9, and 13), early podocyte or parietal epithelium (cluster 14), early parietal epithelium or proximal tubule (cluster 2), parietal epithelium (cluster 11), proximal tubule (cluster 8), and medial/distal precursors (clusters 3, 5, 10, 12, and 15), though variability was observed in the proportional contribution of each batch to individual clusters (Figures 2F–2I).

To compare *in-vitro*-derived cells to cells of the human kidney, we subset 4,405 nephrogenic cells from week-17 human fetal kidney datasets (Tran et al., 2019) and merged the *in-vivo*-with the *in-vitro*-derived nephrogenic cells (Figure 3A). Cluster identification validated the presence of nephrogenic cell types (Figures 3A and 3B; Table S1). Nephron progenitor, nephron segment precursor, late podocyte, and proximal tubule identities were composed of both human fetal kidney and cells of *in vitro* origin, highlighting similarities between the *in vivo* and *in-vitro*-derived cells. Genes exhibiting correlated expression with *MAFB*, *HNF4A*, *SLC12A1*, and *GATA3* in the organoids emphasized expected transcriptional signatures of podocyte (i.e., *PODXL*, *PTPRO*, *NPHS2*, *TCF21*, *CLIC5*, etc.), proximal tubule (i.e., *CUBN*, *LRP2*, *HNF4G*, *SLC3A1*, *SLC34A1*, etc.), loop of Henle (i.e., *TFCP2L1*, *IRX1*, *DEFB1*, *ERBB4*, *MAL*, etc.), and distal precursor (i.e., *CALB1*, *MECOM*, *MAL*, *ALDH1A1*, *EMX2*, etc.) cell identities (Table S1).

Importantly, differences are observed in the transcriptional profiles of *in-vitro*- and *in-vivo*-derived cells (Figures 3A–3D). Cluster 7 (*in vitro* NPCs) and clusters 0 and 15 (*in vitro* podocytes) were predominantly composed of organoid cells. Furthermore, while core TFs driving nephrogenesis marked the segmentation of *in vitro* nephron-like structures (Figure S2E), incomplete maturation was documented in an unbiased comparison with the hu-

man fetal kidney (Table S1; Figures S3A–S3C). For example, *in vitro*-derived podocytes exhibited lower expression of late-activated genes encoding structural proteins or extra cellular matrix components, as previously reported in conventional kidney organoids (e.g., *COL4A4*, *TNNT2*, *DCN*, and *CLXC12*) (Tran et al., 2019; Yoshimura et al., 2019). Generally, solute carriers and transporters mediating key kidney functions were expressed at significantly lower levels in organoid-derived cell types (e.g., *SLC9A3*, *SLC44A3*, *SLC5A2*, and *SLC6A19*) (Figures S3A–S3C; Table S1).

To compare the nephrogenic cells in the organoids in our model with those generated by other groups, we performed an extensive comparative scRNA-seq analysis. We first extracted the nephrogenic lineage single-cell transcriptomes from the published datasets of the human fetal kidney (Tran et al., 2019) and kidney organoids (Combes et al., 2019; Czerniecki et al., 2018; Kumar et al., 2019; Subramanian et al., 2019; Tran et al., 2019; Wu et al., 2018) and then constructed a merged dataset consisting of *in vivo* nephrogenic cells and *in-vitro*-derived cells (from our group and others), using the integration function within Seurat (Figures 3E and 3F). Clusters showed signatures of NPCs, early developing nephron, early and late podocyte, parietal epithelium, proximal tubule, and medial/distal precursors, with contributions from fetal kidney and organoid cells across the different groups (Figures 3G and 3H).

These data support the conclusion of similar differentiation outcomes among PSC-derived organoids profiled by several different groups, including the organoid data presented here, and the clear homology between these *in-vitro*-generated cell types and their *in vivo* counterparts in the developing fetal kidney. However, the merged analysis also highlighted *in-vitro*- and *in-vivo*-specific signatures. Cluster 13 was almost entirely composed of NPCs from the week-17 human kidney, consistent with the absence of NPCs in late-stage kidney organoids (Figures 3G and 3H). Clusters 6 and 17 (early developing nephron) and 10 and 18 (podocyte) were non-overlapping with *in vivo* cells, indicating an *in vitro* difference with *in vivo* cellular programs (Figures 3G and 3H).

We also compared the cellular diversity of the interstitial cell component. Nephron and interstitial progenitors likely share a common origin (Mugford et al., 2008) and may play a role in organizing nephron structures (Das et al., 2013; England et al., 2020). Interstitial cells extracted from the week-17 human fetal kidney data (expressing *MEIS1*, *PDGFRA*, and/or *PDGFRB*) (Tran

**Figure 3. Single-cell transcriptomics-driven comparison of *in vitro* organoid and fetal nephrogenic cells**

- (A) UMAP reduction of integrated nephrogenic cells from kidney organoids and human fetal kidney, colored by clusters, and hierarchical clustering of cell identities.
- (B) Dot plot of marker genes used for cell cluster identification of integrated nephrogenic cells from kidney organoids and the human fetal kidney.
- (C) UMAP reduction of integrated nephrogenic cells from kidney organoids and human fetal kidney, colored by their origins.
- (D) Bar graph of cell count presenting the contribution of different original identities to various clusters of integrated nephrogenic cells from kidney organoids and human fetal kidney.
- (E) UMAP reduction of integrated nephrogenic cells from kidney organoids (of various research groups) and human fetal kidney, colored by clusters, and hierarchical clustering of cell identities.
- (F) Dot plot of marker genes used for cell cluster identification of integrated nephrogenic cells from kidney organoids of various research groups and the human fetal kidney.
- (G) UMAP reduction of integrated nephrogenic cells from kidney organoids of various research groups and human fetal kidney, colored by their origins.
- (H) Bar graph of cell count presenting contribution of different original identities to various clusters of integrated nephrogenic cells from kidney organoids generated by various research groups and human fetal kidney.

See also Figure S3 and Table S1.

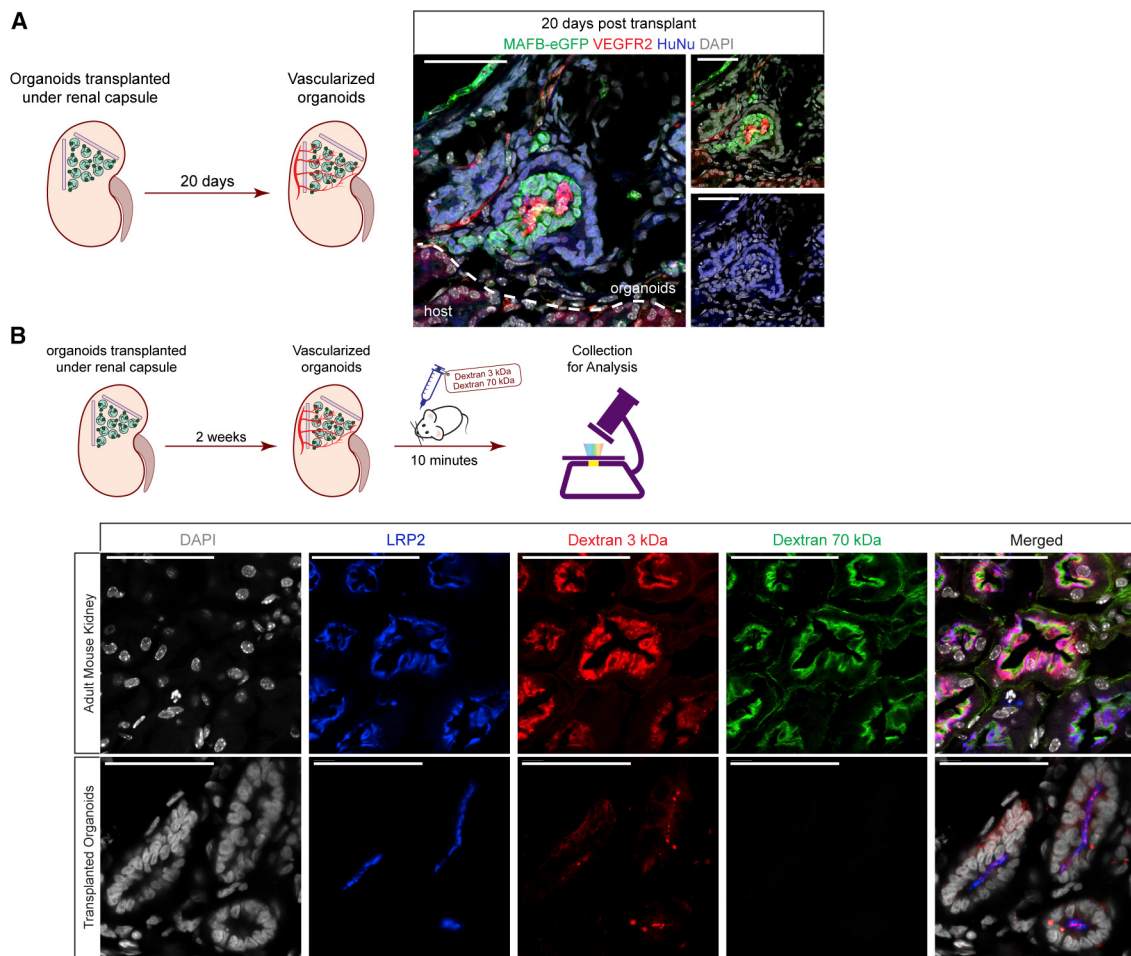


**Figure 4. Vascularization of human kidney organoids**

(A) Left: schematic diagram describing the transplantation procedure to vascularize MAFB-P2A-eGFP organoids. Right: immunofluorescent analyses of cryosectioned vascularized MAFB-P2A-eGFP organoids. Scale bars indicate 50  $\mu$ m.

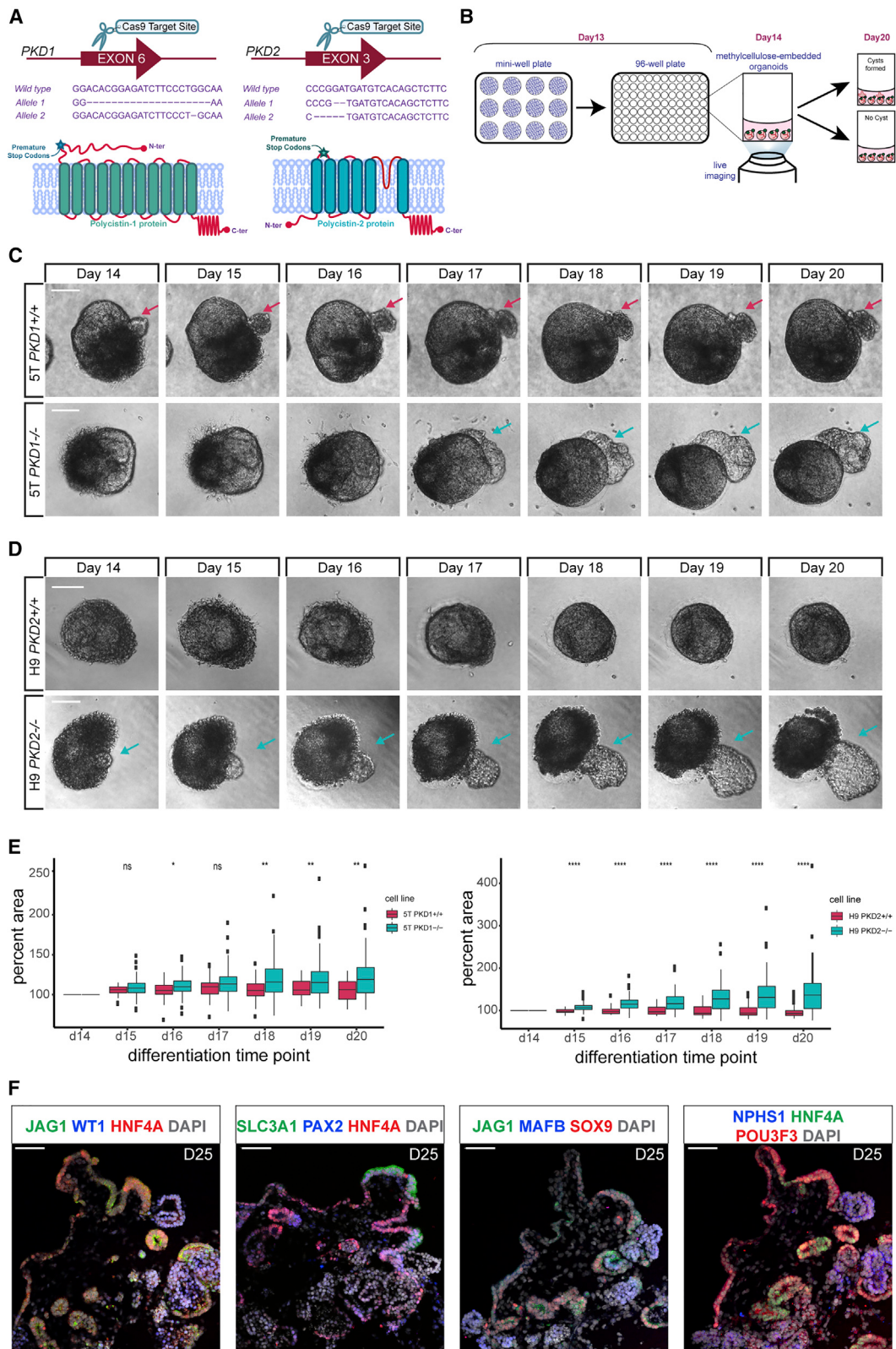
(B) Upper panel: schematic diagram describing the transplantation procedure to vascularize MAFB-P2A-eGFP organoids and injection of Dextran (3 and 70 kDa). Lower panel: immunofluorescent analyses of cryosectioned vascularized MAFB-P2A-eGFP organoids collected 10-min post dye injection. Scale bars indicate 50  $\mu$ m. See also Figure S4.

et al., 2019) generated 14 clusters (Figure S3D). Together with *MEIS1*, *PDGFRA*, and *PDGFRB*, differential expression of *FAM162B*, *LUM*, *KISS1*, *REN*, *TYMS*, *MEF2C*, *MYH1*, *TOP2A*, *COL8A1*, *FOXD1*, *CADM1*, *C7*, *POSTN*, *TAGLN*, *SHISA3*, *DKK1*, *USP53*, *GATA3*, *CCL2*, *IRF1*, *TMX4*, and *GRID2* highlighted the cellular diversity and replicative state of interstitial cells in the developing human kidney (Figure S3E). Merging these data with the organoid scRNA-seq-derived interstitial subset (*MEIS1*, *PDGFRA*, and/or *PDGFRB*) highlighted the absence *in vitro* of specific interstitial subtypes: *COL8A1+/FOXD1+* (cluster 10), *MEF2C+/MYH11+* (cluster 12), and *TMX4+/GRID2+* (cluster 6), and a reduced representation of *CCL2+/IRF1+* (cluster 0), *USP53/GATA3+* (cluster 7), and *TYMS+/MYH11+* (cluster 13) cell types (Figures S3F–S3I), indicating a less complex interstitial cell diversity in the organoid model.

#### Vascularization of kidney organoids

Published organoid models comprising many nephron-like structures have been shown to recruit vasculature and undergo

extended development on grafting to the adult mouse kidney (Tran et al., 2019; van den Berg et al., 2020). To examine the ability of our kidney organoids with just 1–2 nephron-like structures to recruit the vasculature, we transplanted organoids derived from MAFB-P2A-eGFP hESCs under the kidney capsule of non-obese diabetic (NOD)/severe combined immunodeficiency (SCID) mice (Figure 4A). 20 days post-transplant, MAFB+ *in-vitro*-derived podocytes positive for a human nuclear antigen (HuNu+) were surrounded by HuNu– VEGFR2+ mouse endothelial cells (Figure 4A). Vascularized podocytes were PODXL+ and ANXA1+, indicative of mature podocyte-like signatures (Figure S4A; Tran et al., 2019). Proximal tubule-like structures (HNF4A+ CUBN+ LRP2+ ACE2+) were identified in transplanted organoids together with an SLC12A1+ distal tubule-like segment (Figures S4B–S4D). Interestingly, we observed rare SLC12A3+ organoid-derived cells, suggesting additional maturation of distal convoluted tubule cells not observed *in vitro* (Figure S4E). Thus, the kidney organoids demonstrated vascular recruitment, segmented nephron signatures, and the additional maturation of nephron cell types.



(legend on next page)

To evaluate the functional properties of vascularized *in-vitro*-derived nephrons, we performed an *in vivo* dextran uptake assay, injecting Texas-red-conjugated (3 kDa) and tetramethylrhodamine-conjugated (70 kDa) compounds into the retro-orbital venous sinus of the NOD/SCID mice 2 weeks after implanting organoids under the kidney capsule (Figure 4B). Kidneys were collected for analysis 10 min after the injection. As expected, mice injected with PBS showed no fluorescent signature in the kidney (Figure S4F). In the host mouse kidneys, 70-kDa dextran was retained at the apical surface of proximal tubules and in glomerular and peritubular capillaries (Figure 4B; Figure S4F). In contrast, the smaller 3-kDa dextran showed only a weak signal in the glomerular and peritubular capillaries but a strong signal at the apical surface of proximal tubules, consistent with rapid filtering of the smaller dextran molecule (Figure 4B; Figure S4F). Whereas the higher molecular weight compound could not be detected within implanted organoids, the 3-kDa dextran was evident as puncta predominantly associated with the apical region of LRP2+ proximal tubule cells (Figures 4B, S4F, and S4G), consistent with limited vascular permeability and filtering into organoid-derived nephrons.

### Modeling polycystic kidney diseases using kidney organoids

To explore the utility of our scalable organoid platform to model disease and screen for phenotypic modifiers, we generated mutations in the two key genes associated with ADPKD: *PKD1* and *PKD2* (Bergmann et al., 2018; Harris and Torres, 2018). Both mutations were generated through CRISPR-Cas9-directed double-strand DNA cleavage and non-homologous end-joining repair in the H9 hESC line (Figures 5A, S5A, and S5B). Acknowledging the genetic complexity of the *PKD1* gene, which has six known highly homologous pseudogenes (Bogdanova et al., 2001), we designed a guide RNA specific to the bona fide *PKD1* gene sequence (Figure S5A). Sanger sequencing identified clones carrying deletions predicted to generate a loss of function for both alleles of *PKD1* and *PKD2* in distinct targeting events (Figures S5A and S5B). To demonstrate the expected loss of function for each gene, we used validated *PKD1* and *PKD2* antibodies (Yu et al., 2007; MacKay et al., 2020). Wild-type *PKD2* has a predicted molecular weight of 110 kDa but frequently forms higher molecular aggregates in the process of western blot analysis (Yu et al., 2009). *PKD2* protein was detected in wild-type and *PKD1* mutant organoids but not in *PKD2*–/– mutant organoids with biallelic deletions (Figure S5C). *PKD1* encodes a 462-kDa primary polypeptide (PC1), which can be observed on induction of *PKD1* expression in HEK cells (arrowhead in Figure S5D). However, analysis of fetal kidney samples only detects a smaller product of 81 kDa, consistent with published data (Lea et al., 2020), suggesting *in vivo* processing. In control samples and wild-type organoids, a higher

molecular weight (140 kDa) *PKD1* cleavage product was observed, which was lost on biallelic mutation of the *PKD2* gene (arrow in Figure S5E). Thus, both *PKD* mutant clones lost detectable levels of *PKD* protein encoded by the mutated allele (Cai et al., 2014; Hopp et al., 2012; Hu and Harris, 2020; Kim et al., 2014; Kurbegovic et al., 2014; Yu et al., 2007)

To determine whether *PKD* mutant hESC lines can replicate cystic outgrowth, *PKD1*–/– and *PKD2*–/– hESCs were differentiated alongside wild-type hESC lines. Seeding ~1,500 cells/microwell, we examined cyst formation by high-resolution automated imaging of wild-type, *PKD1*, and *PKD2* mutant organoids, cultured in methylcellulose-supplemented medium to prevent movement of the organoids, visualizing cyst growth over multiple days of culture (dd14 to dd20) (Figure 5B; Video S1). qPCR confirmed that *PKD* mutant organoids underwent a similar differentiation trajectory to wild-type hESCs (Figures S5F–S5H). However, in contrast to wild-type organoids, cysts emerged (blue arrows in Figures 5C and 5D) and expanded from *PKD1* and *PKD2* mutant organoids (Figures 5E and 5F).

Cysts were recognizable as early as dd15 and morphologically distinct from low-frequency epithelial protrusions observed in wild-type organoids that grow but do not balloon into cystic structures (red arrow in Figure 5C). Interestingly, cyst formation was dependent on the seeding density; cyst formation was delayed, and cyst frequency decreased, as the number of seeding cells was increased from 1,500 cells to 5,000 or 7,000 cells in the *PKD2*-mutant model (Figures S5I and S5J). Cysts expanded continuously on extended culture, eventually detaching from the parent organoid and generating free-growing cystic structures that reached more than 1 cm in diameter after 3 months of culture (Figure S5K). Antibody profiling showed cystic epithelia displayed a complex profile, with contributions from proximal (JAG1+, HNF4A+, or SLC3A1+) and distal nephron segments (SOX9+ or POU3F3+) (Figures 5F and S5L). Examination of tight junctions (TJP1/ZO-1), an apical polarity marker (PRKCI/aPKC), and the apically localized primary cilium (ARL13B) showed an expected luminal-facing apical polarity of nephric epithelium within the organoid that was reversed in cystic outgrowths with the primary cilium projecting into the culture medium (Denker and Sabath, 2011; Elias et al., 2015; Yoder, 2007; Figure S5M). Polarity reversal has been reported in another *in vitro* model (Cruz et al., 2017), though not in cysts within the kidney of mouse *Pkd* mutants (Ma et al., 2013; Shao et al., 2020; Yu et al., 2008).

### Phenotypic screening to identify protein kinase inhibitors inhibiting cyst initiation

With the advantage of mass production of organoids, we screened an annotated small-molecule protein kinase inhibitor

**Figure 5. Cyst formation in *PKD1*–/– and *PKD2*–/– human kidney organoids**

- (A) Schematic diagram describing the CRISPR-Cas9-induced mutations on *PKD1* or *PKD2* alleles and resulting deletions and frameshifts leading to premature termination of translation.
  - (B) Schematic diagram describing the timeline of the live imaging assay to track cyst formation.
  - (C and D) Bright-field images showing progressive cyst formation from differentiation days 14–20 in *PKD1*–/– or *PKD2*–/– mutant human kidney organoids alongside their wild-type controls. Red arrows: epithelial outpocketing observed at low frequency in wild-type organoids. Blue arrows: forming cysts in *PKD* mutant organoids.
  - (E) Boxplots comparing area increases of *PKD1*–/– or *PKD2*–/– mutants with their isogenic wild-type controls from differentiation days 14–20 (Wilcoxon rank-sum test).
  - (F) Immunofluorescent analyses showing contribution of different nephron segment-like cells to cystic epithelial cells. Scale bars indicate 50 μm.
- See also Figure S5, Table S2, and Video S1.

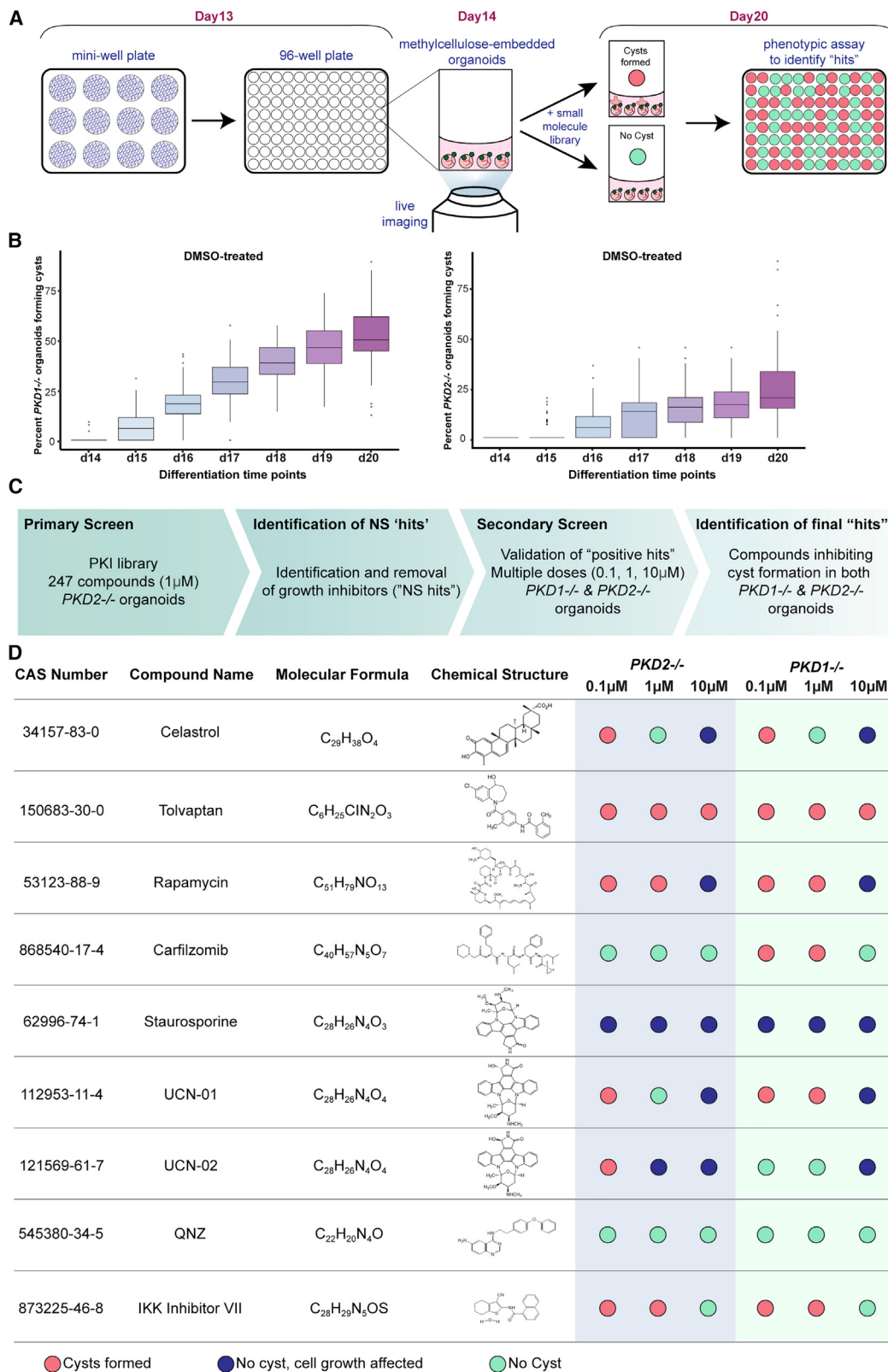


**Figure 6. High-throughput screening to identify compounds inhibiting cyst initiation**

(A) Schematic diagram describing the timeline of the phenotypic assay to identify compounds inhibiting cyst formation.

(B) Quantification of cyst formation rate of DMSO-treated  $PKD1^{-/-}$  or  $PKD2^{-/-}$  organoids from 96 wells of methylcellulose-embedded organoids for each line.

(legend continued on next page)

(PKI) library (see [STAR Methods](#)) to identify potential inhibitors of cyst initiation ([Figure 6A](#)). PKIs can provide broad insight into signaling pathway activities, which may uncover novel mechanisms or avenues for therapeutic approaches beyond the primary PKI hit. Cyst formation was initially calibrated using vehicle (DMSO)-treated *PKD1*<sup>−/−</sup> (n = 933) and *PKD2*<sup>−/−</sup> (n = 1,241) mutant organoids. We performed automated bright-field imaging of each organoid daily from dd14 to dd20. At dd20, 52.3% of *PKD1*<sup>−/−</sup> and 25.3% of *PKD2*<sup>−/−</sup> organoids formed cysts ([Figure 6B](#)). Positive Z scores at dd20 for both the *PKD1*<sup>−/−</sup> and *PKD2*<sup>−/−</sup> lines (0.40 and 0.37, respectively) demonstrated that positive and negative outcomes could be determined with confidence ([Zhang et al., 1999](#); [Figure S6A](#)).

We therefore launched a series of screens to identify PKIs impeding cyst initiation (summarized in [Figure 6C](#)). The primary screen was performed with a library of 247 PKIs, which was assembled by combining the EMD PKI 2, 3, and 4 collections (see [STAR Methods](#)) using a single dose of 1 μM in a primary screen of *PKD2*<sup>−/−</sup> organoids ([Table S2](#)). Approximately 12–15 organoids were screened per well, scoring cyst formation within 9 wells containing each compound, distributed across three separate plates. Cultures were tracked over a 6-day period of culture (dd14–20). Importantly, the compound setup on the plates was blinded from the operator scoring outcomes to reduce operator bias. Screen outcomes were categorized into three groups: (1) “negative hits,” defined as wells with continued cyst formation; (2) “positive hits,” with cyst suppression but continued growth and development of the organoid; and (3) “non-specific hits” (NS hits), with no visible cyst formation but evidence of general growth retardation or cell death ([Figure S6B](#); [Videos S2, S3, and S4](#)). To increase the stringency of the screen, only compounds identified as “positive hits” in all 9 wells for each compound were considered true “hits” and selected for a secondary screen. Among the 247 initial screen compounds, 11 compounds were identified as NS hits and 9 as positive hits ([Table S2](#)).

Hits and various controls ([Table S2](#)) underwent a similarly structured secondary screen on both *PKD1*<sup>−/−</sup> and *PKD2*<sup>−/−</sup> organoids, examining three different concentrations of each compound: 0.1, 1.0, and 10.0 μM. For controls, we included tolvaptan, an inhibitor of AVPR2 and the first FDA-approved pharmacological treatment for ADPKD. Importantly, as AVPR2 is activated in differentiated cells of the connecting segment and collecting duct ([Beaudoin et al., 2019](#); [Higashihara et al., 2011](#); [Hopp et al., 2015](#); [Reif et al., 2011](#); [Torres et al., 2016, 2017](#); [Ransick et al., 2019](#)) that are generally absent from PSC-derived kidney organoids, tolvaptan was not expected to inhibit cyst growth in our assay. The mammalian target of the rapamycin (mTOR) pathway is activated in cystic epithelia in patients with ADPKD and rodent models of polycystic kidney disease. Rapamycin inhibits mTOR in rodent ADPKD models ([Holditch et al., 2019](#); [Shillingford et al., 2010](#); [Tao et al., 2005](#)). Furthermore, rapamycin treatment significantly improved renal function *in vivo* in animal models ([Shillingford et al., 2010](#); [Tao et al., 2005](#)). Therefore, ra-

pamycin was added as a potential inhibitor of cyst formation. Two compounds shown to inhibit cyst formation in ADPKD mouse models: carfilzomib, a proteasome inhibitor, and celastrol, a pentacyclic triterpene ([Booij et al., 2020](#); [Chang et al., 2018](#); [Fedeles et al., 2011](#)), were added as further potential inhibitory controls. Additionally, we also examined the effects of forskolin and blebbistatin, compounds previously identified to enhance cystogenesis ([Czerniecki et al., 2018](#); [Low et al., 2019](#)).

Celastrol, carfilzomib, and rapamycin, but not tolvaptan, scored as positive hits in the secondary screening assay inhibiting cyst formation in *PKD1*<sup>−/−</sup> and *PKD2*<sup>−/−</sup> organoids ([Figure 6D](#)). Carfilzomib inhibited cyst formation at all concentrations evaluated in *PKD2*<sup>−/−</sup> organoids but only at the highest concentration in *PKD1*<sup>−/−</sup> organoids. Neither forskolin or blebbistatin showed any enhancement of cyst outgrowth ([Figures S6C–S6H](#)), though, surprisingly, we observed a significant decrease in growth at the highest concentration but only in the *PKD2* mutant organoid cultures (10 μM; [Figure S6F](#)). Of the compounds identified in the primary *PKD2*<sup>−/−</sup> screen, the protein kinase C (PKC) pathway inhibitors UCN-01 and UCN-02 showed variable results in *PKD1*<sup>−/−</sup> and *PKD2*<sup>−/−</sup> cyst inhibition, whereas quinazoline (QNZ) and IκB kinase (IKK)-inhibitor VII, potential NF-κB pathway modulators ([Tobe et al., 2003](#); [Waelchli et al., 2006](#)), inhibited both *PKD1*<sup>−/−</sup> and *PKD2*<sup>−/−</sup> cyst formation ([Figure 6D](#)). Of note, QNZ prevented cyst formation in both *PKD1* and *PKD2* mutants at all doses.

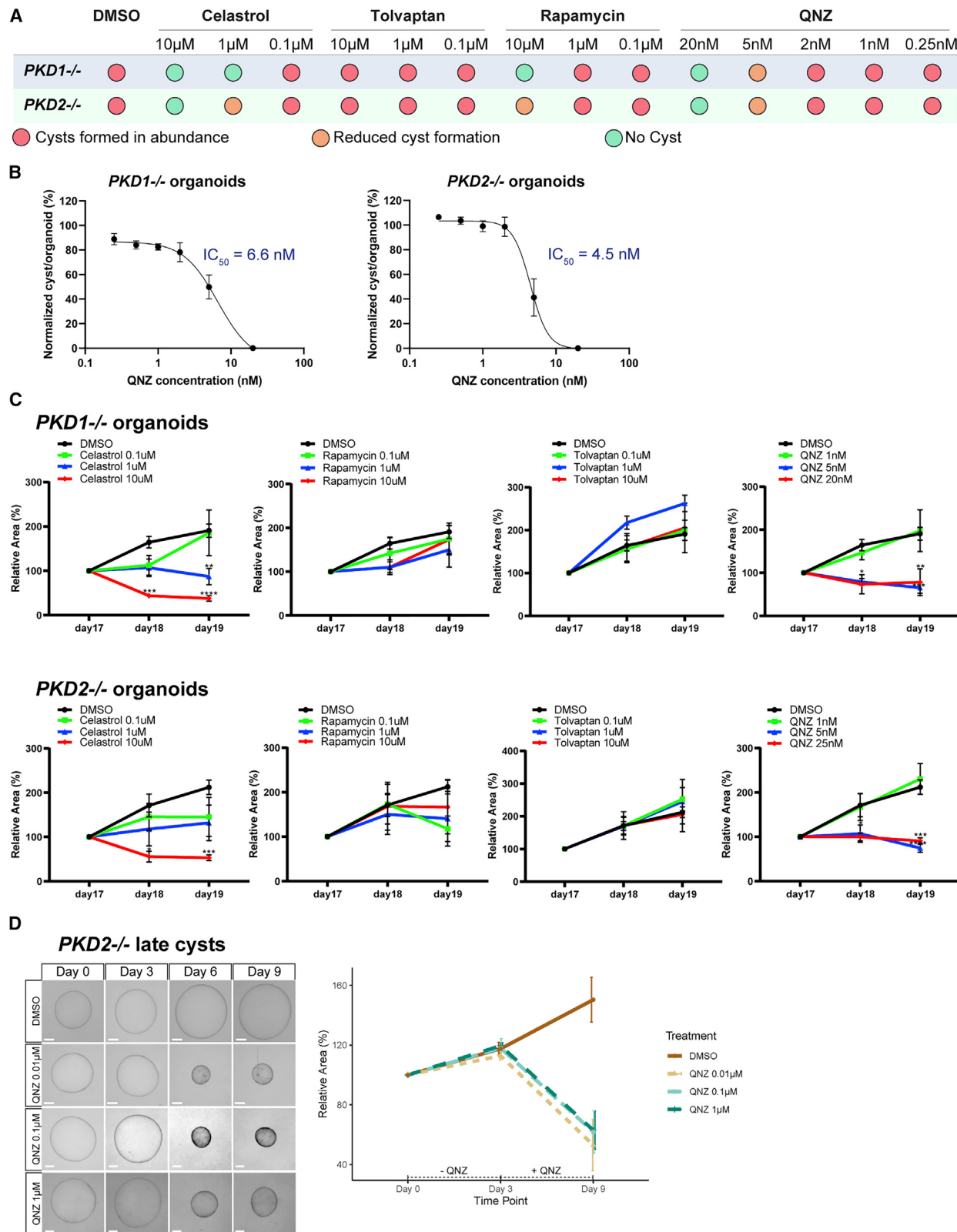
Given the efficacy of QNZ, we examined the effective levels of QNZ for inhibiting cyst formation. Our data showed the concentration-dependent inhibition of cyst formation after QNZ treatment, with an IC<sub>50</sub> of 6.6 nM for the *PKD1* mutant and 4.5 nM for the *PKD2* mutant organoids and a complete inhibition of cyst formation at 20 nM ([Figures 7A and 7B](#)). Next, we examined whether QNZ modified cyst growth after cyst formation had initiated, at early (a few days after cyst initiation) and late (free-growing cysts detached from the organoid) stages. QNZ was added to *PKD1*<sup>−/−</sup> and *PKD2*<sup>−/−</sup> organoids at concentrations ranging from 1 to 25 nM when early cysts were visible (dd16), and cyst outgrowth compared over 2 days of culture together with parallel assays of celastrol, tolvaptan, rapamycin, and a DMSO non-compound control. As expected, DMSO- and tolvaptan-treated organoids underwent cyst expansion, while 10 μM of celastrol reduced cyst areas ([Figure 7C](#)). Rapamycin treatment did not significantly reduce cyst growth in this short-term assay ([Figure 7C](#)). Consistent with the cyst initiation assay, QNZ treatment (5–25 nM) significantly reduced cyst growth in both *PKD1*<sup>−/−</sup> and *PKD2*<sup>−/−</sup> organoids ([Figure 7C](#)). Additionally, QNZ administered to late cysts, (see [STAR Methods](#) for information on late cyst assay; cyst diameter ≥ 1 mm) led to a dramatic reduction in the size of *PKD1*<sup>−/−</sup> (0.1 and 1 μM QNZ) and *PKD2*<sup>−/−</sup> (0.01, 0.1, and 1 μM QNZ) cysts ([Figures 7D and 7A](#)).

Working within the concentration range above, we examined the effects of QNZ on wild-type organoid development. MAFB-eGFP wild-type organoids were treated continuously with QNZ (10 nM–1 μM) over the post aggregation period (from dd8 to

(C) Schematic diagram describing the screening process to identify PKIs impeding cyst formation.

(D) Compounds validated for cyst inhibition in both *PKD1*<sup>−/−</sup> and *PKD2*<sup>−/−</sup> kidney organoids. celastrol, carfilzomib, and rapamycin were included as literature-based positive controls and tolvaptan as a negative control, based on the absence AVPR2 expression.

See also [Figure S6](#), [Table S2](#), and [Videos S2, S3, and S4](#).



(legend on next page)

dd28). Though growth was reduced at the higher concentrations, 10 nM QNZ-treated organoids were comparable in size range to the DMSO control group (Figures S7B and S7C). eGFP+ podocytes first emerged as expected at dd14. Further, qPCR analysis of differentiation markers at the end of the culture period indicated DMSO- and QNZ-treated MAFB-eGFP underwent comparable differentiation (Figure S7D). Transcriptional profiling of organoids at dd28 was consistent with qPCR assays but suggested QNZ treatment initiated metabolic changes and activated stress responses (Figure S7E; Table S1). Transcriptional analysis of PKD2<sup>-/-</sup> organoids (Figure S7F; Table S1) and late cysts (Figure S7G; Table S1) indicated that QNZ affected cell growth and proliferation in addition to inducing stress responses. No significant impact was observed on apoptosis, measured by TUNEL, when organoids were cultured with 20-nM QNZ, a concentration sufficient to block all cyst formation (Figures S7H–S7J). Further, fluorescence-activated cell sorting (FACS) analyses quantifying the percentage of live cells in PKD1 and PKD2 mutant organoids cultured in up to 1-μM QNZ showed no decrease in the live cell FACS index relative to DMSO controls, contrasting with a significant loss of cell viability and marked elevation in apoptosis in kidney cell types treated with 0.1 μM of staurosporine as a positive toxicity control (Figures S7K and S7L). Finally, no significant increase in apoptosis was observed in ZO1+ epithelial cells in late cyst assays treated with 0.01–1 μM QNZ (Figures S7K and S7L). Collectively, these results highlight the potency and specificity of QNZ in inhibiting cyst formation and later growth of independent cystic structures, independent of a marked elevation in apoptosis.

## DISCUSSION

Recognizing the need for a scalable system to generate kidney organoids for developmental studies and translational application, we developed a culture model that provides a good solution to generating tens of thousands of relatively homogenous human kidney organoids of a size and cellular complexity well suited for screening purposes. Although a detailed developmental analysis of nephrogenesis in organoids *in vitro* highlights morphologically distinct structures to those mediating normal nephron formation *in vivo*, our analyses point to similarities in the patterning processes and cellular outcomes. As with all reports of kidney organoid systems, eliminating unwanted cell types and normalizing programs for developmentally and functionally interconnected cell types (vascular, interstitial, and collecting system) will further improve kidney-specific modeling capability.

Utilizing the organoid model, we developed a robust platform to study cyst initiation and expansion in ADPKD. Organoids car-

rying homozygous loss of function in either PKD1 or PKD2 formed reproducible and robust cystic structures, with a more robust cyst-forming capability in the PKD1 mutant organoids. The platform also provides a model for studying aspects of late-stage cystic expansion as cysts continue to grow to centimeter-sized structures, detached from the parental organoid body.

Previous studies have documented cyst formation promoted by small-molecule stimulators of cAMP production in alternative PKD1 and PKD2 PSC-generated organoid models (Czerniecki et al., 2018; Kuraoka et al., 2020; Shimizu et al., 2020). In the absence of stimulation, cysts have been reported in the aforementioned organoid model, albeit at low frequency (~5%). Here, the requirement for manual extraction of cyst-forming organoids from an adherent matrix-encased culture further complicates high-throughput screening (Czerniecki et al., 2018). Cyst formation is clearly assay dependent, as others have not observed cyst formation in an alternative kidney organoid model (Kumar et al., 2019). In our organoid platform, both the timing and frequency of cyst formation depend on the initial seeding density of cells in the kidney organoid aggregate. The percentage of cyst-forming organoids is also markedly improved (25%–50% to ~80%) by adding a preselection based on initial outgrowth at dd14. Coupling machine learning with an organoid-sized sorting system (Pulak, 2006) could generate a highly efficient automated platform for future large-scale screening.

Previous kidney organoid screens identified compounds enhancing cystogenesis: forskolin and 8-bromo-adenosine 3', 5'-cyclic monophosphate (8-Br-cAMP), which elevate intracellular cAMP levels, and blebbistatin, which inhibits myosin ATPase activity (Czerniecki et al., 2018; Low et al., 2019). However, neither forskolin nor blebbistatin enhanced cystogenesis over the time course investigated in our organoid model (Figures S6C–S6H). The model replicated the cyst-inhibitory properties of rapamycin, which has been widely reported to modify cystic growth in ADPKD, although clinical trials of rapamycin in ADPKD patients showed minimal effects on the progression of kidney failure or improved renal function, and strong side-effects of the drug treatment (Serra et al., 2010; Walz et al., 2010). Celesterol and carlfilzomib inhibited cystogenesis in the human kidney organoid model, supporting reports of cyst growth inhibition in transgenic mouse models (Booij et al., 2020; Chang et al., 2018; Fedele et al., 2011; Holditch et al., 2019; Shillingford et al., 2010; Tao et al., 2005).

Screening PKI libraries for compounds suppressing cystogenesis in PKD1<sup>-/-</sup> and PKD2<sup>-/-</sup> kidney organoids sheds new light on inhibitory compounds identifying UCN-01, UCN-02, IKK inhibitor VII, and QNZ as novel inhibitors of cyst formation

## Figure 7. Effects of QNZ on cyst initiation and progressive cyst growth

- (A) Summary of effects of low QNZ doses on inhibiting the initiation of cyst outgrowth in PKD1<sup>-/-</sup> and PKD2<sup>-/-</sup> mutant kidney organoids compared with celestrol, tolvaptan, and rapamycin.
- (B) Determination of IC<sub>50</sub> of QNZ in PKD1<sup>-/-</sup> or PKD2<sup>-/-</sup> organoids, based on cyst formation rates in organoids (data are represented as mean ± SEM).
- (C) Effects of low QNZ doses on inhibition of growth in newly emerged cysts (monitored from dd16 to dd19) arising from PKD1<sup>-/-</sup> and PKD2<sup>-/-</sup> mutant kidney organoids: early cyst inhibition assay. celestrol, tolvaptan, and rapamycin serve as controls (data are represented as mean ± SEM).
- (D) Effects of low QNZ doses on inhibition of growth of cysts arising from free-growing cysts detached from the parent organoid following extended culture: late cyst inhibition assay. QNZ-treated PKD2<sup>-/-</sup> late cysts were compared with DMSO controls from day 0 to day 9 of culture; QNZ administered on day 3 (data are represented as mean ± SEM). Scale bars indicate 500 μm.

See also Figure S7 and Table S1.

in the organoid assay. UCN-01 and UCN-02 are derivatives of PKC-inhibitor staurosporine (Karaman et al., 2008; Rüegg and Gillian, 1989; Takahashi et al., 1989). Staurosporine appeared to generally inhibit cell growth, even at the lowest concentration evaluated (0.1  $\mu$ M), agreeing with previous reports on its role in triggering apoptosis (Bertrand et al., 1994). In contrast, UCN-01 and UCN-02 dose-response experiments point to a more marked effect on cyst growth than general organoid growth, though a more rigorous measure of organoid growth would be required to draw this conclusion. UCN-01 and UCN-02 are stereoisomers, which may explain the different dose-response on PKD1 and PKD2 mutant cysts. UCN-01, UCN-02, and staurosporine have promiscuous kinase inhibition (Tamaoki and Nakano, 1990), so non-PKC mechanisms of action cannot be ruled out.

IKK inhibitor VII is a selective competitive inhibitor of NF- $\kappa$ B signaling, blocking activity of IKKs and transcriptional activation of the NF- $\kappa$ B pathway. IKK inhibitor VII targets both IKK-1 and IKK-2. However, annotated IKK-2-specific kinase inhibitors in the library did not prevent cyst formation in our primary screen suggesting a link to IKK-1 inhibition and potentially non-canonical NF- $\kappa$ B pathway activity in cystogenesis (Table S2). A study of PKD in a rat model has highlighted the expression of noncanonical NF- $\kappa$ B pathway transcriptional components in cystic epithelial cells (Ta et al., 2016).

Interestingly, QNZ, the most effective inhibitory compound identified in our assay, is reported to inhibit NF- $\kappa$ B pathway activation (Scheurer et al., 2019; Tobe et al., 2003), though other studies suggest QNZ indirectly modulates NF- $\kappa$ B signaling through the control of  $\text{Ca}^{2+}$  entry into the cell (Choi et al., 2006). Further, phenotypic screens in Drosophila and an iPSC-derived Huntington's disease model showed QNZ inhibition of neuronal store-operated  $\text{Ca}^{2+}$  entry pathway activity (Nekrasov et al., 2016; Wu et al., 2011). PKD2, a selective cation channel in complex with PKD1, has been linked to primary cilium transport of  $\text{Ca}^{2+}$  and potentially monovalent cations (DeCaen et al., 2013; Kleene and Kleene, 2017; Koulen et al., 2002; Liu et al., 2018; Su et al., 2018). Elevated  $\text{Ca}^{2+}$  levels have been reported in proximal tubule cell cultures from PKD1 mutant mice (Yanda et al., 2019). Our initial transcriptional profiling suggests that QNZ induces stress responses in wild-type organoids, though this response does not inhibit the differentiation of organoids at low cyst-inhibitory doses, and no elevation was observed in apoptosis or FACS-assessed cell viability in either normal or PKD1-mutant organoids, or outgrowing cystic structures, at low QNZ doses that were completely refractory to cyst initiation and cyst growth. Potentially, enhanced stress in PKD-deficient cysts may synergize with QNZ to inhibit cell division at low QNZ concentrations. The strong inhibitory activity of QNZ on cystogenesis at nanomolar concentrations in both *PKD1*–/– and *PKD2*–/– models supports further evaluation of the mechanistic action of this compound for potential therapeutic insight.

In conclusion, the reasonable uniformity in size, cell types, and developmental progression in the kidney organoid platform we describe here are the features well suited to high-throughput, image-based screening. These organoids may also be better suited for renal implantation, and further evaluating functional integration will be an interesting avenue for future studies. In a proof-of-principle, we confirmed cyst inhibition in ADPKD org-

noid kidney models with small-molecule inhibitors active in ADPKD animal models and identified inhibitory compounds. The kidney organoid system we describe complements other approaches to dissect kidney development and study renal functions. Further, our platform adds to existing strategies to identify therapeutic leads for the treatment of ADPKD and potentially other kidney diseases.

### Limitations of the study

The *in vitro* ADPKD model investigates cystogenesis outside of normal kidney function, which may modify cyst-forming pathways. These findings were obtained using an *in vitro* model and need further study to examine the effects of QNZ *in vivo*.

### STAR★METHODS

Detailed methods are provided in the online version of this paper and include the following:

- **KEY RESOURCES TABLE**
- **RESOURCE AVAILABILITY**
  - Lead contact
  - Materials availability
  - Data and code availability
- **EXPERIMENTAL MODEL AND SUBJECT DETAILS**
  - Human kidney studies
  - Human embryonic stem cell lines
- **METHOD DETAILS**
  - Kidney organoid cultures
  - Characterization of the organoid system
  - Vascularization of transplanted kidney organoids
- **QUANTIFICATION AND STATISTICAL ANALYSIS**

### SUPPLEMENTAL INFORMATION

Supplemental information can be found online at <https://doi.org/10.1016/j.stem.2022.06.005>.

### ACKNOWLEDGMENTS

We appreciate the help from Dr. Andrew Ransick, Kari Koppitch, and Jinjin Guo with scRNA-seq sample preparation using 10X Genomics technology and validations, and members of the McMahon laboratory for insightful scientific discussions. We are grateful to the Choi family for their generous donation to establish the Choi Family Therapeutic Screening Center that enabled the small-molecule screens in this study and to Mickey Huang for assistance in the screening process. C.J.S. was supported by the Amgen-USC Postdoctoral Fellowship Program. T.T. was supported by the T32 Training Grant in Developmental Biology, Stem Cells and Regeneration from NICHD (T32HD060549). Work in A.P.M.'s laboratory was supported by a grant from NIDDK (DK054364).

### AUTHOR CONTRIBUTIONS

T.T., C.J.S., D.C.-H.L., and A.P.M. designed experiments. T.T., C.J.S., T.N., S.-Y.C., J.A.M., R.Y., B.D., S.Y.C., and N.O.L. performed the experiments, data collection and/or data analysis. T.T., C.J.S., and A.P.M. wrote the manuscript and incorporated collaborator, manuscript reviewer, and editorial inputs.

### DECLARATION OF INTERESTS

A.P.M. receives consulting fees or stock options for his scientific advisory role for eGENESIS, TRESTLE BioTherapeutics, and IVIVA Medical. Amgen Inc.

supports a USC-Amgen Scholar's program, and C.J.S. is funded through this program. A.P.M., C.J.S., and T.T. have applied for intellectual property protection on work presented here (patent pending).

#### INCLUSION AND DIVERSITY

One or more of the authors of this paper self-identifies as an underrepresented ethnic minority in science. While citing references scientifically relevant for this work, we also actively worked to promote gender balance in our reference list.

Received: December 24, 2020

Revised: January 28, 2022

Accepted: June 8, 2022

Published: July 7, 2022

#### REFERENCES

- Asawa, R.R., Danchik, C., Zahkarov, A., Chen, Y., Voss, T., Jadhav, A., Wallace, D.P., Trott, J.F., Weiss, R.H., Simeonov, A., et al. (2020). A high-throughput screening platform for Polycystic Kidney Disease (PKD) drug repurposing utilizing murine and human ADPKD cells. *Sci. Rep.* **10**, 4203.
- Basta, J.M., Robbins, L., Kiefer, S.M., Dorsett, D., and Rauchman, M. (2014). Sall1 balances self-renewal and differentiation of renal progenitor cells. *Development* **141**, 1047–1058.
- Beaudoin, J.J., Bezencon, J., Cao, Y., Mizuno, K., Roth, S.E., Brock, W.J., and Brouwer, K.L.R. (2019). Altered hepatobiliary disposition of tolvaptan and selected tolvaptan metabolites in a rodent model of polycystic kidney disease. *Drug Metab. Dispos.* **47**, 155–163.
- Becht, E., McInnes, L., Healy, J., Dutertre, C.A., Kwok, I.W.H., Ng, L.G., Ginhoux, F., and Newell, E.W. (2018). Dimensionality reduction for visualizing single-cell data using UMAP. *Nat. Biotechnol.* <https://doi.org/10.1038/nbt.4314>.
- Bergmann, C., Guay-Woodford, L.M., Harris, P.C., Horie, S., Peters, D.J.M., and Torres, V.E. (2018). Polycystic kidney disease. *Nat. Rev. Dis. Primers* **4**, 50.
- Berry, R.L., Ozdemir, D.D., Aronow, B., Lindström, N.O., Dudnakova, T., Thornburn, A., Perry, P., Baldock, R., Armit, C., Joshi, A., et al. (2015). Deducing the stage of origin of Wilms' tumours from a developmental series of *Wt1*-mutant mice. *Dis. Model. Mech.* **8**, 903–917.
- Bertrand, R., Solary, E., O'Connor, P., Kohn, K.W., and Pommier, Y. (1994). Induction of a common pathway of apoptosis by staurosporine. *Exp. Cell Res.* **211**, 314–321.
- Bogdanova, N., Markoff, A., Gerke, V., McCluskey, M., Horst, J., and Dworniczak, B. (2001). Homologues to the first gene for autosomal dominant polycystic kidney disease are pseudogenes. *Genomics* **74**, 333–341.
- Booij, T.H., Bange, H., Leonhard, W.N., Yan, K., Fokkelman, M., Kunnen, S.J., Dauwense, J.G., Qin, Y., van de Water, B., van Westen, G.J.P., et al. (2017). High-throughput phenotypic screening of kinase inhibitors to identify drug targets for polycystic kidney disease. *SLAS Discov.* **22**, 974–984.
- Booij, T.H., Leonhard, W.N., Bange, H., Yan, K., Fokkelman, M., Plugge, A.J., Veraar, K.A.M., Dauwense, J.G., van Westen, G.J.P., van de Water, B., et al. (2020). *In vitro* 3D phenotypic drug screen identifies celastrol as an effective *in vivo* inhibitor of polycystic kidney disease. *J. Mol. Cell Biol.* **12**, 644–653.
- Cai, Y., Fedele, S.V., Dong, K., Anyatonwu, G., Onoe, T., Mitobe, M., Gao, J.D., Okuhara, D., Tian, X., Gallagher, A.R., et al. (2014). Altered trafficking and stability of polycystins underlie polycystic kidney disease. *J. Clin. Invest.* **124**, 5129–5144.
- Cao, J., O'Day, D.R., Pliner, H.A., Kingsley, P.D., Deng, M., Daza, R.M., Zager, M.A., Aldinger, K.A., Blecher-Gonen, R., Zhang, F., et al. (2020). A human cell atlas of fetal gene expression. *Science* **370**, eaba7721.
- Chang, M.Y., Hsieh, C.Y., Lin, C.Y., Chen, T.D., Yang, H.Y., Chen, K.H., Hsu, H.H., Tian, Y.C., Chen, Y.C., Hung, C.C., et al. (2018). Effect of celastrol on the progression of polycystic kidney disease in a *Pkd1*-deficient mouse model. *Life Sci.* **212**, 70–79.
- Choi, S., Kim, J.H., Roh, E.J., Ko, M.J., Jung, J.E., and Kim, H.J. (2006). Nuclear factor-kappaB activated by capacitative Ca<sup>2+</sup> entry enhances muscarinic receptor-mediated soluble amyloid precursor protein (sAPPalpha) release in SH-SY5Y cells. *J. Biol. Chem.* **281**, 12722–12728.
- Cirio, M.C., Hui, Z., Haldin, C.E., Cosentino, C.C., Stuckenholz, C., Chen, X., Hong, S.K., Dawid, I.B., and Hukriede, N.A. (2011). Lhx1 is required for specification of the renal progenitor cell field. *PLoS One* **6**, e18858.
- Combes, A.N., Zappia, L., Er, P.X., Oshlack, A., and Little, M.H. (2019). Single-cell analysis reveals congruence between kidney organoids and human fetal kidney. *Genome Med.* **11**, 3.
- Cruz, N.M., Song, X., Czerniecki, S.M., Gulieva, R.E., Churchill, A.J., Kim, Y.K., Winston, K., Tran, L.M., Diaz, M.A., Fu, H., et al. (2017). Organoid cystogenesis reveals a critical role of microenvironment in human polycystic kidney disease. *Nat. Mater.* **16**, 1112–1119.
- Czerniecki, S.M., Cruz, N.M., Harder, J.L., Menon, R., Annis, J., Otto, E.A., Gulieva, R.E., Islas, L.V., Kim, Y.K., Tran, L.M., et al. (2018). High-throughput screening enhances kidney organoid differentiation from human pluripotent stem cells and enables automated multidimensional phenotyping. *Cell Stem Cell* **22**, 929–940.e4.
- Das, A., Tanigawa, S., Karner, C.M., Xin, M., Lum, L., Chen, C., Olson, E.N., Perantoni, A.O., and Carroll, T.J. (2013). Stromal–epithelial crosstalk regulates kidney progenitor cell differentiation. *Nat. Cell Biol.* **15**, 1035–1044.
- DeCaen, P.G., Delling, M., Vien, T.N., and Clapham, D.E. (2013). Direct recording and molecular identification of the calcium channel of primary cilia. *Nature* **504**, 315–318.
- Denker, B.M., and Sabath, E. (2011). The biology of epithelial cell tight junctions in the kidney. *J. Am. Soc. Nephrol.* **22**, 622–625.
- Dobin, A., Davis, C.A., Schlesinger, F., Drenkow, J., Zaleski, C., Jha, S., Batut, P., Chaisson, M., and Gingeras, T.R. (2013). STAR: ultrafast universal RNA-seq aligner. *Bioinformatics* **29**, 15–21.
- Elias, B.C., Das, A., Parekh, D.V., Mernaugh, G., Adams, R., Yang, Z., Brakebusch, C., Pozzi, A., Marciano, D.K., Carroll, T.J., et al. (2015). Cdc42 regulates epithelial cell polarity and cytoskeletal function during kidney tubule development. *J. Cell Sci.* **128**, 4293–4305.
- England, A.R., Chaney, C.P., Das, A., Patel, M., Malewska, A., Armendariz, D., Hon, G.C., Strand, D.W., Drake, K.A., and Carroll, T.J. (2020). Identification and characterization of cellular heterogeneity within the developing renal interstitium. *Development* **147**, dev190108.
- Fedeles, S.V., Tian, X., Gallagher, A.R., Mitobe, M., Nishio, S., Lee, S.H., Cai, Y., Geng, L., Crews, C.M., and Somlo, S. (2011). A genetic interaction network of five genes for human polycystic kidney and liver diseases defines polycystin-1 as the central determinant of cyst formation. *Nat. Genet.* **43**, 639–647.
- Forbes, T.A., Howden, S.E., Lawlor, K., Phipson, B., Maksimovic, J., Hale, L., Wilson, S., Quinlan, C., Ho, G., Holman, K., et al. (2018). Patient-iPSC-derived kidney organoids show functional validation of a ciliopathic renal phenotype and reveal underlying pathogenetic mechanisms. *Am. J. Hum. Genet.* **102**, 816–831.
- Freedman, B.S., Brooks, C.R., Lam, A.Q., Fu, H., Morizane, R., Agrawal, V., Saad, A.F., Li, M.K., Hughes, M.R., Werff, R.V., et al. (2015). Modelling kidney disease with CRISPR-mutant kidney organoids derived from human pluripotent epiblast spheroids. *Nat. Commun.* **6**, 8715.
- Grote, D., Souabni, A., Busslinger, M., and Bouchard, M. (2006). Pax 2/8-regulated Gata 3 expression is necessary for morphogenesis and guidance of the nephric duct in the developing kidney. *Development* **133**, 53–61.
- Guo, G., Morrison, D.J., Licht, J.D., and Quaggin, S.E. (2004). WT1 activates a glomerular-specific enhancer identified from the human nephrin gene. *J. Am. Soc. Nephrol.* **15**, 2851–2856.
- Hale, L.J., Howden, S.E., Phipson, B., Lonsdale, A., Er, P.X., Ghobrial, I., Hosawi, S., Wilson, S., Lawlor, K.T., Khan, S., et al. (2018). 3D organoid-derived human glomeruli for personalised podocyte disease modelling and drug screening. *Nat. Commun.* **9**, 5167.
- Harris, P.C., and Torres, V.E. (2018). Polycystic kidney disease, autosomal dominant. In *GeneReviews®*, M.P. Adam, H.H. Ardinger, R.A. Pagon, S.E. Wallace, L.J.H. Bean, K.W. Gripp, G.M. Mirzaa, and A. Amemiya, eds. (University of Washington).

- Hartwig, S., Ho, J., Pandey, P., Macisaac, K., Taglienti, M., Xiang, M., Alterovitz, G., Ramoni, M., Fraenkel, E., and Kreidberg, J.A. (2010). Genomic characterization of Wilms' tumor suppressor 1 targets in nephron progenitor cells during kidney development. *Development* 137, 1189–1203.
- Heliot, C., Desgrange, A., Buisson, I., Prunskaitė-Hyryläinen, R., Shan, J., Vainio, S., Umbhauer, M., and Cereghini, S. (2013). HNF1B controls proximal-intermediate nephron segment identity in vertebrates by regulating Notch signalling components and Irx1/2. *Development* 140, 873–885.
- Higashihara, E., Torres, V.E., Chapman, A.B., Grantham, J.J., Bae, K., Watnick, T.J., Horie, S., Nutahara, K., Ouyang, J., Krasa, H.B., et al. (2011). Tolvaptan in autosomal dominant polycystic kidney disease: three years' experience. *Clin. J. Am. Soc. Nephrol.* 6, 2499–2507.
- Hochane, M., van den Berg, P.R., Fan, X., Bérenger-Currias, N., Adegeest, E., Bialecka, M., Nieveen, M., Menschaert, M., Chuva de Sousa Lopes, S.M., and Semrau, S. (2019). Single-cell transcriptomics reveals gene expression dynamics of human fetal kidney development. *PLoS Biol.* 17, e3000152.
- Holditch, S.J., Brown, C.N., Atwood, D.J., Lombardi, A.M., Nguyen, K.N., Toll, H.W., Hopp, K., and Edelstein, C.L. (2019). A study of sirolimus and mTOR kinase inhibitor in a hypomorphic Pkd1 mouse model of autosomal dominant polycystic kidney disease. *Am. J. Physiol. Ren. Physiol.* 317, F187–F196.
- Hopp, K., Hommerding, C.J., Wang, X., Ye, H., Harris, P.C., and Torres, V.E. (2015). Tolvaptan plus pasireotide shows enhanced efficacy in a PKD1 model. *J. Am. Soc. Nephrol.* 26, 39–47.
- Hopp, K., Ward, C.J., Hommerding, C.J., Nasr, S.H., Tuan, H.F., Gainullin, V.G., Rossetti, S., Torres, V.E., and Harris, P.C. (2012). Functional polycystin-1 dosage governs autosomal dominant polycystic kidney disease severity. *J. Clin. Invest.* 122, 4257–4273.
- Howden, S.E., Vanslambrouck, J.M., Wilson, S.B., Tan, K.S., and Little, M.H. (2019). Reporter-based fate mapping in human kidney organoids confirms nephron lineage relationships and reveals synchronous nephron formation. *EMBO Rep.* 20, e47483.
- Howden, S.E., Wilson, S.B., Groenewegen, E., Starks, L., Forbes, T.A., Tan, K.S., Vanslambrouck, J.M., Holloway, E.M., Chen, Y.H., Jain, S., et al. (2021). Plasticity of distal nephron epithelia from human kidney organoids enables the induction of ureteric tip and stalk. *Cell Stem Cell* 28, 671–684.e6.
- Hu, J., and Harris, P.C. (2020). Regulation of polycystin expression, maturation and trafficking. *Cell. Signal.* 72, 109630.
- Jinek, M., Chylinski, K., Fonfara, I., Hauer, M., Doudna, J.A., and Charpentier, E. (2012). A programmable dual-RNA-guided DNA endonuclease in adaptive bacterial immunity. *Science* 337, 816–821.
- Johansen, K.L., Chertow, G.M., Foley, R.N., Gilbertson, D.T., Herzog, C.A., Ishani, A., Israni, A.K., Ku, E., Kurella Tamura, M., Li, S., et al. (2021). US renal data system 2020 annual data report: epidemiology of kidney disease in the United States. *Am. J. Kidney Dis.* 77, A7–A8.
- Kann, M., Ettou, S., Jung, Y.L., Lenz, M.O., Taglienti, M.E., Park, P.J., Schermer, B., Benzing, T., and Kreidberg, J.A. (2015). Genome-wide analysis of Wilms' tumor 1-controlled gene expression in podocytes reveals key regulatory mechanisms. *J. Am. Soc. Nephrol.* 26, 2097–2104.
- Karaman, M.W., Herrgard, S., Treiber, D.K., Gallant, P., Atteridge, C.E., Campbell, B.T., Chan, K.W., Ciceri, P., Davis, M.I., Edeen, P.T., et al. (2008). A quantitative analysis of kinase inhibitor selectivity. *Nat. Biotechnol.* 26, 127–132.
- Kim, A.D., Lake, B.B., Chen, S., Wu, Y., Guo, J., Parvez, R.K., Tran, T., Thornton, M.E., Grubbs, B., McMahon, J.A., et al. (2019). Cellular recruitment by podocyte-derived pro-migratory factors in assembly of the human renal filter. *iScience* 20, 402–414.
- Kim, H., Xu, H., Yao, Q., Li, W., Huang, Q., Outeda, P., Cebotaru, V., Chiaravalli, M., Boletta, A., Piontek, K., et al. (2014). Ciliary membrane proteins traffic through the Golgi via a Rabep1/GGA1/Arl3-dependent mechanism. *Nat. Commun.* 5, 5482.
- Kim, Y.K., Refaeli, I., Brooks, C.R., Jing, P., Gulieva, R.E., Hughes, M.R., Cruz, N.M., Liu, Y., Churchill, A.J., Wang, Y., et al. (2017). Gene-edited human kidney organoids reveal mechanisms of disease in podocyte development. *Stem Cells* 35, 2366–2378.
- Kleene, S.J., and Kleene, N.K. (2017). The native TRPP2-dependent channel of murine renal primary cilia. *Am. J. Physiol. Ren. Physiol.* 312, F96–F108.
- Kobayashi, A., Kwan, K.M., Carroll, T.J., McMahon, A.P., Mendelsohn, C.L., and Behringer, R.R. (2005). Distinct and sequential tissue-specific activities of the LIM-class homeobox gene Lim1 for tubular morphogenesis during kidney development. *Development* 132, 2809–2823.
- Kobayashi, A., Valerius, M.T., Mugford, J.W., Carroll, T.J., Self, M., Oliver, G., and McMahon, A.P. (2008). Six2 defines and regulates a multipotent self-renewing nephron progenitor population throughout mammalian kidney development. *Cell Stem Cell* 3, 169–181.
- Koulen, P., Cai, Y., Geng, L., Maeda, Y., Nishimura, S., Witzgall, R., Ehrlich, B.E., and Somlo, S. (2002). Polycystin-2 is an intracellular calcium release channel. *Nat. Cell Biol.* 4, 191–197.
- Kumar, S.V., Er, P.X., Lawlor, K.T., Motazedian, A., Scurr, M., Ghobrial, I., Combes, A.N., Zappia, L., Oshlack, A., Stanley, E.G., et al. (2019). Kidney micro-organoids in suspension culture as a scalable source of human pluripotent stem cell-derived kidney cells. *Development* 146, dev172361.
- Kume, T., Deng, K., and Hogan, B.L. (2000). Murine forkhead/winged helix genes Foxc1 (Mf1) and Foxc2 (Mfh1) are required for the early organogenesis of the kidney and urinary tract. *Development* 127, 1387–1395.
- Kuraoka, S., Tanigawa, S., Taguchi, A., Hotta, A., Nakazato, H., Osafune, K., Kobayashi, A., and Nishinakamura, R. (2020). PKD1-dependent renal cystogenesis in human induced pluripotent stem cell-derived ureteric bud/collecting duct organoids. *J. Am. Soc. Nephrol.* 31, 2355–2371.
- Kurbegovic, A., Kim, H., Xu, H., Yu, S., Cruanès, J., Maser, R.L., Boletta, A., Trudel, M., and Qian, F. (2014). Novel functional complexity of polycystin-1 by GPS cleavage in vivo: role in polycystic kidney disease. *Mol. Cell. Biol.* 34, 3341–3353.
- Lam, A.Q., Freedman, B.S., Morizane, R., Lerou, P.H., Valerius, M.T., and Bonventre, J.V. (2014). Rapid and efficient differentiation of human pluripotent stem cells into intermediate mesoderm that forms tubules expressing kidney proximal tubular markers. *J. Am. Soc. Nephrol.* 25, 1211–1225.
- Lea, W.A., McGreal, K., Sharma, M., Parnell, S.C., Zelenchuk, L., Charlesworth, M.C., Madden, B.J., Johnson, K.L., McCormick, D.J., Hogan, M.C., et al. (2020). Analysis of the polycystin complex (PCC) in human urinary exosome-like vesicles (ELVs). *Sci. Rep.* 10, 1500.
- Liao, Y., Smyth, G.K., and Shi, W. (2014). featureCounts: an efficient general purpose program for assigning sequence reads to genomic features. *Bioinformatics* 30, 923–930.
- Lindström, N.O., De Sena Brandine, G., Tran, T., Ransick, A., Suh, G., Guo, J., Kim, A.D., Parvez, R.K., Ruffins, S.W., Rutledge, E.A., et al. (2018a). Progressive recruitment of mesenchymal progenitors reveals a time-dependent process of cell fate acquisition in mouse and human nephrogenesis. *Dev. Cell* 45, 651–660.e4.
- Lindström, N.O., De Sena Brandine, G., Ransick, A., Suh, G., Guo, J., Kim, A.D., Parvez, R.K., Thornton, M.E., Baskin, L., et al. (2018b). Conserved and divergent features of mesenchymal progenitor cell types within the cortical nephrogenic niche of the human and mouse kidney. *J. Am. Soc. Nephrol.* 29, 806–824.
- Lindström, N.O., McMahon, J.A., Guo, J., Tran, T., Guo, Q., De Sena Brandine, G., Ransick, A., Parvez, R.K., Thornton, M.E., Baskin, L., et al. (2018c). Conserved and divergent features of human and mouse kidney organogenesis. *J. Am. Soc. Nephrol.* 29, 785–805.
- Lindström, N.O., Sealoff, R., Chen, X., Parvez, R.K., Ransick, A., De Sena Brandine, G., Guo, J., Hill, B., Tran, T., Kim, A.D., et al. (2021). Spatial transcriptional mapping of the human nephrogenic program. *Dev. Cell* 56, 2381–2398.e6.
- Lindström, N.O., Tran, T., Guo, J., Rutledge, E., Parvez, R.K., Thornton, M.E., Grubbs, B., McMahon, J.A., and McMahon, A.P. (2018d). Conserved and divergent molecular and anatomic features of human and mouse nephron patterning. *J. Am. Soc. Nephrol.* 29, 825–840.
- Liu, X., Vien, T., Duan, J., Sheu, S.H., DeCaen, P.G., and Clapham, D.E. (2018). Polycystin-2 is an essential ion channel subunit in the primary cilium of the renal collecting duct epithelium. *eLife* 7, e33183.

- Love, M.I., Huber, W., and Anders, S. (2014). Moderated estimation of fold change and dispersion for RNA-seq data with DESeq2. *Genome Biol.* 15, 550.
- Low, J.H., Li, P., Chew, E.G.Y., Zhou, B., Suzuki, K., Zhang, T., Lian, M.M., Liu, M., Aizawa, E., Rodriguez Esteban, C., et al. (2019). Generation of human PSC-derived kidney organoids with patterned nephron segments and a de novo vascular network. *Cell Stem Cell* 25, 373–387.e9.
- Ma, M., Tian, X., Igarashi, P., Pazour, G.J., and Somlo, S. (2013). Loss of cilia suppresses cyst growth in genetic models of autosomal dominant polycystic kidney disease. *Nat. Genet.* 45, 1004–1012.
- MacKay, C.E., Leo, M.D., Fernández-Peña, C., Hasan, R., Yin, W., Mata-Daboin, A., Bulley, S., Gammons, J., Mancarella, S., and Jaggar, J.H. (2020). Intravascular flow stimulates PKD2 (polycystin-2) channels in endothelial cells to reduce blood pressure. *eLife* 9, e56655.
- Marable, S.S., Chung, E., Adam, M., Potter, S.S., and Park, J.S. (2018). Hnf4a deletion in the mouse kidney phenocopies Fanconi renotubular syndrome. *JCI Insight* 3, e97497.
- Menon, R., Otto, E.A., Kokoruda, A., Zhou, J., Zhang, Z., Yoon, E., Chen, Y.C., Troyanskaya, O., Spence, J.R., Kretzler, M., et al. (2018). Single-cell analysis of progenitor cell dynamics and lineage specification in the human fetal kidney. *Development* 145, dev164038.
- Moriguchi, T., Hamada, M., Morito, N., Terunuma, T., Hasegawa, K., Zhang, C., Yokomizo, T., Esaki, R., Kuroda, E., Yoh, K., et al. (2006). MafB is essential for renal development and F4/80 expression in macrophages. *Mol. Cell. Biol.* 26, 5715–5727.
- Morizane, R., and Bonventre, J.V. (2017). Generation of nephron progenitor cells and kidney organoids from human pluripotent stem cells. *Nat. Protoc.* 12, 195–207.
- Morizane, R., Lam, A.Q., Freedman, B.S., Kishi, S., Valerius, M.T., and Bonventre, J.V. (2015). Nephron organoids derived from human pluripotent stem cells model kidney development and injury. *Nat. Biotechnol.* 33, 1193–1200.
- Motojima, M., Kume, T., and Matsusaka, T. (2017). Foxc1 and Foxc2 are necessary to maintain glomerular podocytes. *Exp. Cell Res.* 352, 265–272.
- Mugford, J.W., Sipilä, P., McMahon, J.A., and McMahon, A.P. (2008). Osr1 expression demarcates a multi-potent population of intermediate mesoderm that undergoes progressive restriction to an Osr1-dependent nephron progenitor compartment within the mammalian kidney. *Dev. Biol.* 324, 88–98.
- Naiman, N., Fujioka, K., Fujino, M., Valerius, M.T., Potter, S.S., McMahon, A.P., and Kobayashi, A. (2017). Repression of interstitial identity in nephron progenitor cells by Pax2 establishes the nephron-interstitium boundary during kidney development. *Dev. Cell* 41, 349–365.e3.
- Nakai, S., Sugitani, Y., Sato, H., Ito, S., Miura, Y., Ogawa, M., Nishi, M., Jishage, K., Minowa, O., and Noda, T. (2003). Crucial roles of Brn1 in distal tubule formation and function in mouse kidney. *Development* 130, 4751–4759.
- Naylor, R.W., Przepiorski, A., Ren, Q., Yu, J., and Davidson, A.J. (2013). HNF1beta is essential for nephron segmentation during nephrogenesis. *J. Am. Soc. Nephrol.* 24, 77–87.
- Nekrasov, E.D., Vigont, V.A., Klyushnikov, S.A., Lebedeva, O.S., Vassina, E.M., Bogomazova, A.N., Chestkov, I.V., Semashko, T.A., Kiseleva, E., Suldina, L.A., et al. (2016). Manifestation of Huntington's disease pathology in human induced pluripotent stem cell-derived neurons. *Mol. Neurodegener.* 11, 27.
- Nyengaard, J.R., and Bendtsen, T.F. (1992). Glomerular number and size in relation to age, kidney weight, and body surface in normal man. *Anat. Rec.* 232, 194–201.
- O'Rahilly, R., and Müller, F. (2010). Developmental stages in human embryos: revised and new measurements. *Cells Tissues Organs* 192, 73–84.
- O'Rahilly, R., Müller, F., Hutchins, G.M., and Moore, G.W. (1987). Computer ranking of the sequence of appearance of 73 features of the brain and related structures in staged human embryos during the sixth week of development. *Am. J. Anat.* 180, 69–86.
- Park, J.S., Ma, W., O'Brien, L.L., Chung, E., Guo, J.J., Cheng, J.G., Valerius, M.T., McMahon, J.A., Wong, W.H., and McMahon, A.P. (2012). Six2 and Wnt regulate self-renewal and commitment of nephron progenitors through shared gene regulatory networks. *Dev. Cell* 23, 637–651.
- Przepiorski, A., Sander, V., Tran, T., Hollywood, J.A., Sorrenson, B., Shih, J.H., Wolvetang, E.J., McMahon, A.P., Holm, T.M., and Davidson, A.J. (2018). A simple bioreactor-based method to generate kidney organoids from pluripotent stem cells. *Stem Cell Rep.* 11, 470–484.
- Pulak, R. (2006). Techniques for analysis, sorting, and dispensing of *C. elegans* on the COPAS flow-sorting system. *Methods Mol. Biol.* 351, 275–286.
- Qi, L.S., Larson, M.H., Gilbert, L.A., Doudna, J.A., Weissman, J.S., Arkin, A.P., and Lim, W.A. (2013). Repurposing CRISPR as an RNA-guided platform for sequence-specific control of gene expression. *Cell* 152, 1173–1183.
- Ransick, A., Lindström, N.O., Liu, J., Zhu, Q., Guo, J.J., Alvarado, G.F., Kim, A.D., Black, H.G., Kim, J., and McMahon, A.P. (2019). Single-cell profiling reveals sex, lineage, and regional diversity in the mouse kidney. *Dev. Cell* 51, 399–413.e7.
- Reginensi, A., Clarkson, M., Neirijnck, Y., Lu, B., Ohyama, T., Groves, A.K., Sock, E., Wegner, M., Costantini, F., Chaboissier, M.C., et al. (2011). SOX9 controls epithelial branching by activating RET effector genes during kidney development. *Hum. Mol. Genet.* 20, 1143–1153.
- Reif, G.A., Yamaguchi, T., Nivens, E., Fujiki, H., Pinto, C.S., and Wallace, D.P. (2011). Tolvaptan inhibits ERK-dependent cell proliferation, Cl<sup>-</sup> secretion, and in vitro cyst growth of human ADPKD cells stimulated by vasopressin. *Am. J. Physiol. Ren. Physiol.* 301, F1005–F1013.
- Robinson, M.D., McCarthy, D.J., and Smyth, G.K. (2010). edgeR: a Bioconductor package for differential expression analysis of digital gene expression data. *Bioinformatics* 26, 139–140.
- Rüegg, U.T., and Burgess, G.M. (1989). Staurosporine, K-252 and UCN-01: potent but nonspecific inhibitors of protein kinases. *Trends Pharmacol. Sci.* 10, 218–220.
- Sadl, V., Jin, F., Yu, J., Cui, S., Holmyard, D., Quaggin, S., Barsh, G., and Cordes, S. (2002). The mouse Kreisler (Krm1/MafB) segmentation gene is required for differentiation of glomerular visceral epithelial cells. *Dev. Biol.* 249, 16–29.
- Sasaki, T., Tsuboi, N., Okabayashi, Y., Haruhara, K., Kanzaki, G., Koike, K., Kobayashi, A., Yamamoto, I., Takahashi, S., Ninomiya, T., et al. (2019). Estimation of nephron number in living humans by combining unenhanced computed tomography with biopsy-based stereology. *Sci. Rep.* 9, 14400.
- Sato, H., Idiris, A., Miwa, T., and Kumagai, H. (2016). Microfabric vessels for embryoid body formation and rapid differentiation of pluripotent stem cells. *Sci. Rep.* 6, 31063.
- Scheurer, M.J.J., Brands, R.C., El-Mesery, M., Hartmann, S., Müller-Richter, U.D.A., Kübler, A.C., and Seher, A. (2019). The selection of NFκappaB inhibitors to block inflammation and induce sensitisation to FASL-induced apoptosis in HNSCC cell lines is critical for their use as a prospective cancer therapy. *Int. J. Mol. Sci.* 20, 1306.
- Self, M., Lagutin, O.V., Bowling, B., Hendrix, J., Cai, Y., Dressler, G.R., and Oliver, G. (2006). Six2 is required for suppression of nephrogenesis and progenitor renewal in the developing kidney. *EMBO J.* 25, 5214–5228.
- Serra, A.L., Poster, D., Kistler, A.D., Krauer, F., Raina, S., Young, J., Rentsch, K.M., Spanaus, K.S., Senn, O., Kristanto, P., et al. (2010). Sirolimus and kidney growth in autosomal dominant polycystic kidney disease. *N. Engl. J. Med.* 363, 820–829.
- Shao, L., El-Jouni, W., Kong, F., Ramesh, J., Kumar, R.S., Shen, X., Ren, J., Devendra, S., Dorschel, A., Wu, M., et al. (2020). Genetic reduction of cilium length by targeting intraflagellar transport 88 protein impedes kidney and liver cyst formation in mouse models of autosomal polycystic kidney disease. *Kidney Int.* 98, 1225–1241.
- Shillingford, J.M., Piontek, K.B., Germino, G.G., and Weimbs, T. (2010). Rapamycin ameliorates PKD resulting from conditional inactivation of Pkd1. *J. Am. Soc. Nephrol.* 21, 489–497.
- Shimizu, T., Mae, S.I., Araoka, T., Okita, K., Hotta, A., Yamagata, K., and Osafune, K. (2020). A novel ADPKD model using kidney organoids derived from disease-specific human iPSCs. *Biochem. Biophys. Res. Commun.* 529, 1186–1194.

- Skarnes, W.C., Ning, G., Giansiracusa, S., Cruz, A.S., Blauwendraat, C., Saavedra, B., Holden, K., Cookson, M.R., Ward, M.E., and McDonough, J.A. (2021). Controlling homology-directed repair outcomes in human stem cells with dCas9. Preprint at bioRxiv. <https://doi.org/10.1101/2021.12.16.472942>.
- Stuart, T., Butler, A., Hoffman, P., Hafemeister, C., Papalexopoulou, A., Mauck, W.M., Hao, Y., Stoeckius, M., Smibert, P., and Satija, R. (2019). Comprehensive integration of single-cell data. *Cell* 177, 1888–1902.e21.
- Su, Q., Hu, F., Ge, X., Lei, J., Yu, S., Wang, T., Zhou, Q., Mei, C., and Shi, Y. (2018). Structure of the human PKD1-PKD2 complex. *Science* 361, eaat9819.
- Subramanian, A., Sidhom, E.H., Emani, M., Vernon, K., Sahakian, N., Zhou, Y., Kost-Alimova, M., Slyper, M., Waldman, J., Dionne, D., et al. (2019). Single cell census of human kidney organoids shows reproducibility and diminished off-target cells after transplantation. *Nat. Commun.* 10, 5462.
- Ta, M.H., Schwensen, K.G., Liuwantara, D., Huso, D.L., Watnick, T., and Rangan, G.K. (2016). Constitutive renal Rel/nuclear factor-kappaB expression in Lewis polycystic kidney disease rats. *World J. Nephrol.* 5, 339–357.
- Taguchi, A., Kaku, Y., Ohmori, T., Sharmin, S., Ogawa, M., Sasaki, H., and Nishinakamura, R. (2014). Redefining the in vivo origin of metanephric nephron progenitors enables generation of complex kidney structures from pluripotent stem cells. *Cell Stem Cell* 14, 53–67.
- Taguchi, A., and Nishinakamura, R. (2017). Higher-order kidney organogenesis from pluripotent stem cells. *Cell Stem Cell* 21, 730–746.e6.
- Takahashi, I., Asano, K., Kawamoto, I., Tamaoki, T., and Nakano, H. (1989). UCN-01 and UCN-02, new selective inhibitors of protein kinase C. I. Screening, producing organism and fermentation. *J. Antibiot. (Tokyo)* 42, 564–570.
- Takasato, M., Er, P.X., Becroft, M., Vanslambrouck, J.M., Stanley, E.G., Elefanty, A.G., and Little, M.H. (2014). Directing human embryonic stem cell differentiation towards a renal lineage generates a self-organizing kidney. *Nat. Cell Biol.* 16, 118–126.
- Takasato, M., Er, P.X., Chiu, H.S., Maier, B., Baillie, G.J., Ferguson, C., Parton, R.G., Wolvetang, E.J., Roost, M.S., Chuva de Sousa Lopes, S.M., et al. (2015). Kidney organoids from human iPS cells contain multiple lineages and model human nephrogenesis. *Nature* 526, 564–568.
- Tamaoki, T., and Nakano, H. (1990). Potent and specific inhibitors of protein kinase C of microbial origin. *Biotechnology. (N Y)* 8, 732–735.
- Tao, Y., Kim, J., Schrier, R.W., and Edelstein, C.L. (2005). Rapamycin markedly slows disease progression in a rat model of polycystic kidney disease. *J. Am. Soc. Nephrol.* 16, 46–51.
- Thomas, R., Kanso, A., and Sedor, J.R. (2008). Chronic kidney disease and its complications. *Prim. Care* 35, 329–344.
- Tobe, M., Isobe, Y., Tomizawa, H., Nagasaki, T., Takahashi, H., Fukazawa, T., and Hayashi, H. (2003). Discovery of quinazolines as a novel structural class of potent inhibitors of NF-κappa B activation. *Bioorg. Med. Chem.* 11, 383–391.
- Torres, V.E., Chapman, A.B., Devuyst, O., Gansevoort, R.T., Perrone, R.D., Koch, G., Ouyang, J., McQuade, R.D., Blais, J.D., Czerwic, F.S., et al. (2017). Tolvaptan in later-stage autosomal dominant polycystic kidney disease. *N. Engl. J. Med.* 377, 1930–1942.
- Torres, V.E., Higashihara, E., Devuyst, O., Chapman, A.B., Gansevoort, R.T., Grantham, J.J., Perrone, R.D., Ouyang, J., Blais, J.D., Czerwic, F.S., et al. (2016). Effect of tolvaptan in autosomal dominant polycystic kidney disease by CKD stage: results from the TEMPO 3:4 trial. *Clin. J. Am. Soc. Nephrol.* 11, 803–811.
- Tran, T., Lindström, N.O., Ransick, A., De Sena Brandine, G., Guo, Q., Kim, A.D., Der, B., Peti-Peterdi, J., Smith, A.D., Thornton, M., et al. (2019). In vivo developmental trajectories of human podocyte inform in vitro differentiation of pluripotent stem cell-derived podocytes. *Dev. Cell* 50, 102–116.e6.
- Uchimura, K., Wu, H., Yoshimura, Y., and Humphreys, B.D. (2020). Human pluripotent stem cell-derived kidney organoids with improved collecting duct maturation and injury modeling. *Cell Rep.* 33, 108514.
- van den Berg, C.W., Koudijs, A., Ritsma, L., and Rabelink, T.J. (2020). In vivo assessment of size-selective glomerular sieving in transplanted human induced pluripotent stem cell-derived kidney organoids. *J. Am. Soc. Nephrol.* 31, 921–929.
- van den Berg, C.W., Ritsma, L., Avramut, M.C., Wiersma, L.E., van den Berg, B.M., Leuning, D.G., Lievers, E., Koning, M., Vanslambrouck, J.M., Koster, A.J., et al. (2018). Renal subcapsular transplantation of PSC-derived kidney organoids induces Neo-vasculogenesis and significant glomerular and tubular maturation in vivo. *Stem Cell Rep.* 10, 751–765.
- Waelchli, R., Bollbuck, B., Bruns, C., Buhl, T., Eder, J., Feifel, R., Hersperger, R., Janser, P., Revesz, L., Zerwes, H.G., et al. (2006). Design and preparation of 2-benzamido-pyrimidines as inhibitors of IKK. *Bioorg. Med. Chem. Lett.* 16, 108–112.
- Walz, G., Budde, K., Mannaa, M., Nürnberger, J., Wanner, C., Sommerer, C., Kunzendorf, U., Banas, B., Hörl, W.H., Obermüller, N., et al. (2010). Everolimus in patients with autosomal dominant polycystic kidney disease. *N. Engl. J. Med.* 363, 830–840.
- Wu, H., Uchimura, K., Donnelly, E.L., Kiritani, Y., Morris, S.A., and Humphreys, B.D. (2018). Comparative analysis and refinement of human PSC-derived kidney organoid differentiation with single-cell transcriptomics. *Cell Stem Cell* 23, 869–881.e8.
- Wu, J., Shih, H.P., Vigont, V., Hrdlicka, L., Diggins, L., Singh, C., Mahoney, M., Chesworth, R., Shapiro, G., Zimina, O., et al. (2011). Neuronal store-operated calcium entry pathway as a novel therapeutic target for Huntington's disease treatment. *Chem. Biol.* 18, 777–793.
- Xinaris, C., Benedetti, V., Rizzo, P., Abbate, M., Corna, D., Azzollini, N., Conti, S., Unbekandt, M., Davies, J.A., Morigi, M., et al. (2012). In vivo maturation of functional renal organoids formed from embryonic cell suspensions. *J. Am. Soc. Nephrol.* 23, 1857–1868.
- Xu, P.X., Adams, J., Peters, H., Brown, M.C., Heaney, S., and Maas, R. (1999). Eya1-deficient mice lack ears and kidneys and show abnormal apoptosis of organ primordia. *Nat. Genet.* 23, 113–117.
- Xu, P.X., Zheng, W., Huang, L., Maire, P., Laclef, C., and Silvius, D. (2003). Six1 is required for the early organogenesis of mammalian kidney. *Development* 130, 3085–3094.
- Yanda, M.K., Liu, Q., Cebotaru, V., Guggino, W.B., and Cebotaru, L. (2019). Role of calcium in adult onset polycystic kidney disease. *Cell. Signal.* 53, 140–150.
- Yoder, B.K. (2007). Role of primary cilia in the pathogenesis of polycystic kidney disease. *J. Am. Soc. Nephrol.* 18, 1381–1388.
- Yoshimura, Y., Taguchi, A., and Nishinakamura, R. (2017). Generation of a three-dimensional kidney structure from pluripotent stem cells. *Methods Mol. Biol.* 1597, 179–193.
- Yoshimura, Y., Taguchi, A., Tanigawa, S., Yatsuda, J., Kamba, T., Takahashi, S., Kurihara, H., Mukoyama, M., and Nishinakamura, R. (2019). Manipulation of nephron-patterning signals enables selective induction of podocytes from human pluripotent stem cells. *J. Am. Soc. Nephrol.* 30, 304–321.
- Yu, A.S., Kanzawa, S.A., Usorov, A., Lantinga-van Leeuwen, I.S., and Peters, D.J. (2008). Tight junction composition is altered in the epithelium of polycystic kidneys. *J. Pathol.* 216, 120–128.
- Yu, G., Wang, L.G., Han, Y., and He, Q.Y. (2012). clusterProfiler: an R package for comparing biological themes among gene clusters. *Omics* 16, 284–287.
- Yu, S., Hackmann, K., Gao, J., He, X., Piontek, K., García-González, M.A., Menezes, L.F., Xu, H., Germino, G.G., Zuo, J., et al. (2007). Essential role of cleavage of Polycystin-1 at G protein-coupled receptor proteolytic site for kidney tubular structure. *Proc. Natl. Acad. Sci. USA* 104, 18688–18693.
- Yu, Y., Ulbrich, M.H., Li, M.H., Buraei, Z., Chen, X.Z., Ong, A.C., Tong, L., Isacoff, E.Y., and Yang, J. (2009). Structural and molecular basis of the assembly of the TRPP2/PKD1 complex. *Proc. Natl. Acad. Sci. USA* 106, 11558–11563.
- Zhang, J.H., Chung, T.D., and Oldenburg, K.R. (1999). A simple statistical parameter for use in evaluation and validation of high throughput screening assays. *J. Biomol. Screen.* 4, 67–73.

## STAR★METHODS

## KEY RESOURCES TABLE

REAGENT or RESOURCE	SOURCE	IDENTIFIER
<b>Antibodies</b>		
WT1	abcam	ab89901; RRID: AB_2043201
JAG1	R&D	AF599; RRID: AB_2128257
LAMB1	Santa Cruz	sc-33709; RRID: AB_627868
SOX9	abcam	ab185230; RRID: AB_2715497
HNF4A	R&D	MAB4605
CUBN	R&D	AF3700; RRID: AB_2086138
SLC12A1	Sigma	HPA018107; RRID: AB_1854504
LTL	Vector Laboratories	FL-1321; RRID: AB_2336559
SLC3A1	Sigma	HPA038360; RRID: AB_2675975
NPHS1	abcam	ab136927
POU3F3	ThermoFisher	PA5-64311; RRID: AB_2645790
MAFB	R&D	MAB3810; RRID: AB_2137675
PAX8	abcam	ab189249; RRID: AB_2801268
CDH1	Biosciences	610182; RRID: AB_397581
PAX2	R&D	AF3364; RRID: AB_10889828
GATA3	R&D	AF2605; RRID: AB_2108571
ACE2	R&D	AF933; RRID: AB_355722
PKD1	Kerafast ( <a href="#">Yu et al., 2007</a> )	EMD303
PKD2	Santa Cruz	sc-28331; RRID: AB_672377
DRAQ5	Novus Biologicals	NBP2-81125-50ul
DAPI	ThermoFisher	D1306, RRID: AB_2629482
<b>Chemicals, peptides, and recombinant proteins</b>		
<i>Bacillus licheniformis</i> cold active protease	Creative Enzymes	NATE-0633
Collagenase type 2	Worthington	#LS00417
DNase I	Worthington	#LS002058
AutoMACS Running Buffer	Miltenyl Biotec	130-091-221
Methylcellulose powder	Sigma-Aldrich	M0512
CHIR99021	Sigma Aldrich	SML1046
ActivinA	R&D	338-AC-050
FGF9	R&D	279-F9
Click-iT Plus TUNEL Assay	Invitrogen	C10618
EMD-Protein Kinase Inhibitor 2	EMD Calbiochem®	539745
EMD-Protein Kinase Inhibitor 3	EMD Calbiochem®	539746
EMD-Protein Kinase Inhibitor 4	EMD Calbiochem®	539747
<b>Critical commercial assays</b>		
10x Genomics Chromium Single Cell 3' GEM, Library & Gel Bead Kit	10X Genomics	PN-1000075
HiSeq 3000/4000 SBS PE clustering kit	Illumina	PE-410-001
150 cycle flow cell	Illumina	FC-410-1002
<b>Deposited data</b>		
scRNA-seq of Kidney Organoids	This study	GEO: GSE164564
Bulk RNA-seq of PKD mutant kidney organoids and cysts	This study	GEO: GSE195717
scRNA-seq of Kidney Organoids	<a href="#">Czerniecki et al., 2018</a>	GEO: GSE109718

(Continued on next page)

**Continued**

REAGENT or RESOURCE	SOURCE	IDENTIFIER
scRNA-seq of Kidney Organoids	Subramanian et al., 2019	GEO: GSE136314
scRNA-seq of Kidney Organoids	Wu et al., 2018	GEO: GSE118184
scRNA-seq of Kidney Organoids	Combes et al., 2019	GEO: GSE114802
scRNA-seq of Kidney Organoids	Kumar et al., 2019	GEO: GSE117211
scRNA-seq of Kidney Organoids	Tran et al., 2019	GEO: GSE124472
scRNA-seq of Human Fetal Kidney (Week 17)	Tran et al., 2019	GEO: GSE124472
<b>Experimental models: Cell lines</b>		
H9 hESC	WiCell	WA09
PKD2-/- H9 hESC	This paper	N/A
5T H9 hESC	This paper	N/A
5T PKD1-/- H9 hESC	This paper	N/A
MAFB-P2A-eGFP H9 hESC	Tran et al., 2019	N/A
KOLF2.1J iPSC	Skarnes et al., 2021	N/A
<b>Experimental models: Organisms/strains</b>		
Immunocompromised mice	The Jackson Laboratory	NOD.CB17-Prkdc<SCID>/J, RRID: MGI:5652139
<b>Oligonucleotides</b>		
gRNA PKD1 (TGGCAACGGGCA CTGCTACC)	This paper	N/A
gRNA PKD2 (CCCGGATGATGTC ACAGCTCTTC)	This paper	N/A
Primer1_PKD1_Sanger_seq_ genotype (TCCAGATGGGGCAGAGCCTG)	This paper	N/A
Primer2_PKD1_Sanger_seq_ genotype (CCTCCTTCCTCCTGAGACTC)	This paper	N/A
Primer1_PKD2_Sanger_seq_ genotype (CTGTGTTCCAGTGACCTACG)	This paper	N/A
Primer2_PKD2_Sanger_seq_ genotype (AAGGCACAGGCCAAAGTTCTCA)	This paper	N/A
<b>Software and algorithms</b>		
Seurat 3.0	Stuart et al., 2019	<a href="http://satijalab.org/seurat/">http://satijalab.org/seurat/</a>
CellRanger 3.1	10x Genomics	<a href="https://support.10xgenomics.com">https://support.10xgenomics.com</a>

## RESOURCE AVAILABILITY

### Lead contact

Further information and requests for resources and reagents should be directed to and will be fulfilled by the lead contact, Dr. Andrew P. McMahon ([amcmahon@med.usc.edu](mailto:amcmahon@med.usc.edu)).

### Materials availability

Cell lines generated in this study can be shared upon request following submission of a Material Transfer Agreement.

### Data and code availability

Single-cell RNA-seq datasets collected in this study have been deposited at GEO, and accession number has been detailed in the [key resources table](#).

This paper uses referenced sources of code; no novel code was created for the analyzes in this study. Details of key parameters are provided in the [method details](#) section. If additional information is required for reanalysis of the data reported here, the [lead contact](#) will provide the information on request.

## EXPERIMENTAL MODEL AND SUBJECT DETAILS

### Human kidney studies

Collection of de-identified human fetal tissue from elective terminations with informed consent was approved by the Institutional Review Boards of both Children's Hospital of Los Angeles and the Keck School of Medicine of the University of Southern California.

Guidelines from the American College of Obstetricians and Gynecologists were used to determine the gestational age using a combination of ultrasound and last menstrual measurements (O'Rahilly and Müller, 2010; O'Rahilly et al., 1987). Samples were transported on ice at 4°C in high glucose DMEM (Gibco, 11965-118) supplemented with 10% fetal bovine serum (Genesee Scientific, 25-550) and 25mM HEPES (Gibco, 15630080).

### Human embryonic stem cell lines

H9 hESC line (female) was obtained from WiCell (WA09). CRISPR-Cas9 gene-editing (Jinek et al., 2012; Qi et al., 2013) was adopted to generate the *PKD1*-/- and *PKD2*-/- H9 hESC lines. For *PKD2* mutation, a gRNA (5'-CCCGGATGATGTCACAGCTCTTC-3') targeting coding sequences in exon 3 was delivered to H9 hESCs together with Cas9 protein (Thermofisher MPK5000S) by electroporation. Targeted hESCs were dissociated into single cells using Accutase (Gibco, A1110501) and seeded on a Geltrex-coated 96-well plate at 1 cell/well density, in mTeSR (StemCell Technologies, 85850) supplemented with 10 µM Y27632 (Tocris, 1254). Single cell-derived colonies were expanded and targeting events analyzed by qPCR and validated by Sanger sequencing (see below).

The *PKD1*-/- H9 line was generated using CRISPR-Cas9 technology on the background of a fluorescent reporter line generated on the H9 line background to visualize different components of the nephron (5-T H9 ESCs, shortened here to 5-T). *PKD1* was targeted with a gRNA (5'-TGGCAACGGGCCTGCTACC-3') homologous to sequences in coding exon 6 of the *PKD1* gene. Clonal targeted colonies were identified similar to the *PKD2*-/- hESC line.

Kolf2.1J iPSC line was a gift from Dr. William Skarnes (Skarnes et al., 2021).

## METHOD DETAILS

### Kidney organoid cultures

#### hPSC maintenance

**Geltrex-coated plate preparation.** DMEM/F12 (Life Technologies, 11320-033) was aliquoted into a 50-ml conical vial and 120µl of Geltrex added to make a 1% Geltrex mix. After thorough mixing, 2ml of 1% Geltrex was pipetted into each well of a 6-well plate (or 1ml/well for a 12-well plate). The Geltrex plates were incubated at 37°C/5% CO<sub>2</sub> overnight before use.

**hPSC expansion and maintenance.** This study utilized six hPSC lines (listed in [key resources table](#)) (Tran et al., 2019). hPSCs were thawed in StemFit media (Ajinomoto, ASB01-R) supplemented with 100ng/ml of FGF2 (R&D, 273-F9) and 10µM Y27632 (Tocris, 1254) on 1% Geltrex-coated plates (ThermoFisher, A1413302). On reaching 70-80% confluence (1-2 days), cells were passaged in StemFit media + 100ng/ml of FGF2 + 10µM Y27632 into a 12-well plate at a seeding density of 6,000 cells/well. The medium was changed 48 hours later to StemFit media + 100ng/ml of FGF2 for cell expansion and replenished every 2 days. For freezing, when wells reached 70-80% confluence each well of hPSCs was mixed with 1ml of 10% DMSO/90% fetal bovine serum (FBS) and stored in insulated styrofoam boxes at -80°C overnight before transferring to liquid nitrogen storage.

#### Directed differentiation to generate kidney organoids

The differentiation protocol was developed based on published protocols (Morizane et al., 2015; Morizane and Bonventre, 2017) adapted in our laboratory. Each biological replicate was generated from a distinct frozen vial of hPSCs. After thawing and growth to 70% confluence, hPSCs were dissociated using Accutase (Gibco, A1110501) and seeded on 12-well plates and cultured as above. The differentiation procedure was initiated at 60% confluence. Briefly, culture medium was supplement for 4 days with 8µM CHIR99021 (Sigma Aldrich, SML1046) for differentiation of all hESC lines (or 7µM CHIR99021 for the kolf2.1 iPSC line), followed by 3 days with 10ng/ml ActivinA (R&D, 338-AC-050), and 1 day of 10ng/ml FGF9 incubation (R&D, 273-F9). At day 8, the cells were dissociated using TrypLE dissociation enzyme (Gibco, 12563011), and 600,000 cells seeded into each well of a 12-well EZSPHERE plate (Nacalai USA, TCI-4815-903SP-50P) in 3µM CHIR and 10ng/ml FGF9. Each well generated ~400 organoids and each organoid comprised ~1,500 cells. On differentiation day (dd) 10, the medium was switched to Advanced RPMI 1640 (Gibco, 12633020) + 1X Glutamax (Gibco, 35050079) + 1% Penicillin-Streptomycin (Invitrogen, 15070063), denoted basal differentiation medium, with 10ng/ml FGF9. From dd13 to dd28, cultures were maintained in basal differentiation medium. For the kolf2.1 iPSC differentiation, Essential 6 (Gibco, A1516401) was used as the basal differentiation medium.

#### Validation of *PKD1* and *PKD2* mutant alleles

Single cell-derived clones of the *PKD1* and *PKD2* targeted hESC lines were expanded and genomic DNA was extracted using the DNeasy Blood & Tissue Kit (Qiagen, 69504). CRISPR-Cas9 targeted regions were amplified using the Q5 High-Fidelity 2X Master Mix (*PKD1*: primers: 5'-TCCAGATGGGGCAGAGCCTG-3' and 5'-CCTCCTCCTGAGACTC-3' and *PKD2*: 5'-CTGTGTTCCAGT GACCTACG-3', and 5'-AAGGCACAGGCAAAGTTCTCA-3'), and cloned into the pCR™-Blunt II-TOPO™ vector using the Zero Blunt™ TOPO™ PCR Cloning Kit (Invitrogen K280002). The inserted TOPO plasmids were expanded and Sanger sequencing performed to validate CRISPR mutations on each allele.

#### Embedding of kidney organoids for observation and phenotypic drug screening

**Preparation of methylcellulose plates.** To prepare cultures for fixed organoid tracking over time, 15g of methylcellulose powder (Sigma-Aldrich, M0512) was autoclaved in a 500-ml Erlenmeyer flask. The autoclaved methylcellulose was dissolved in 60°C 450 ml of Advanced RPMI 1640 Medium (Gibco, 12633020). Fifty milliliters of Advanced RPMI 1640 Medium + 1X Glutamax (Gibco, 35050079) and 1% Penicillin-Streptomycin (Invitrogen, 15070063) was then added at room temperature to a final volume of 500ml and a stock concentration of 30 µg/ml methylcellulose. The final stock solution was cleared by centrifugation at 4000 x g for 2 hours. For organoid culture and imaging, 34 µl of the 30 µg/ml methylcellulose stock solution was added to 136 µl of basal differentiation

media to each well of a 96-well plate (brand) to achieve the final concentration of 6 µg/ml methylcellulose optimal for organoid embedding.

*Organoid embedding for growth assays.* At dd13, kidney organoids were transferred from the EZSPHERE plates to a sterile 35-mm dish by gentle pipetting with wide-bore P1000 tips. Under a dissecting microscope, 10-12 organoids were picked up in 10 µl of media and released into methylcellulose in a single well of the imaging plate.

#### Protein kinase inhibitor PKD screening of human kidney organoid cultures

*Protein kinase inhibitor library and additional small molecule compounds.* Two hundred and forty-seven annotated small molecule protein kinase inhibitory compounds were screened at 1 µM in the primary screen. Purchased compounds represented the following commercial libraries: EMD-Protein Kinase Inhibitor 2 (EMD Calbiochem®, Catalog no. 539745), EMD-Protein Kinase Inhibitor 3 (EMD Calbiochem®, Catalog no. 539746), EMD-Protein Kinase Inhibitor 4 (EMD Calbiochem®, Catalog no. 539747).

*Primary screen.* Protein kinase inhibitors were diluted in DMSO to generate 10 µM stocks. At dd14, 20 µl of each diluted compound or DMSO was added to a methylcellulose well with embedded organoids (180 µl of media) to achieve a final concentration of 1 µM. The plates were loaded onto an ImageXpress Micro System for live imaging throughout the screening period. The imaging was performed using the “Standard” algorithm, at 4X magnification, 2 camera binning, with laser-based and image-based focusing enabled, and well-to-well autofocus was set to “focus on plate bottom and well bottom”. To avoid observer bias, we performed blinded experiments in which the compound maps were not revealed to the researcher processing the ImageXpress output until all analyses were completed.

*Scoring phenotypes.* Initially, we screened organoids generated from the *PKD2*-/- hESC line with the full compound library set. We categorized the outcomes of compound treatments into 3 groups: 1) “no-hit” wells were cyst formation and growth appeared normal at dd20 (cyst area  $\geq$ 30% organoid size), 2) “hit” wells in which no cyst formation was observed but epithelial structures remained healthy, and 3) “non-specific hit” (NS hit) wells were no cyst formation occurred but there was clear evidence of cell death and general growth retardation in the culture.

*Secondary screen.* Compounds scored as “hits” in the primary *PKD2*-/- focused screen were selected for validation in a secondary screen inhibiting cyst initiation in *PKD1*-/- and *PKD2*-/- mutant organoids testing a concentration range of each small molecule along with “no hit” and “NS-hit” controls. At dd14, 20 µl of each diluted compound stock or DMSO was added to a methylcellulose well with embedded organoids (180 µl) to achieve a final concentration of 0.1, 1 or 10 µM (with the exception of UCN-01, which was examined at 0.2, 2 or 20 µM). The plates were imaged for 7 days using the ImageXpress Micro System as described above. Compounds that inhibit cyst formation in both *PKD1*-/- and *PKD2*-/- organoids were classified as final “hits”.

To determine the lowest concentration of QNZ capable of inhibiting cyst initiation, *PKD1*-/- and *PKD2*-/- mutant organoids were embedded as described previously, and were treated with QNZ at 0.25, 1, 2, 5 and 20 nM.

*Effects of QNZ on early and late cyst growth.* To assay the effects of compounds on early cyst growth shortly after cyst initiation, dd15, *PKD1*-/- and *PKD2*-/- mutant organoids with recognizable tubular protrusions were embedded in methylcellulose wells. The organoids were treated with DMSO, Celastrol (0.1, 1 and 10 µM), Tolvaptan (0.1, 1 and 10 µM), Rapamycin (0.1, 1 and 10 µM), or QNZ (0.25, 1, 2, 5 and 20 nM) at dd16, and were imaged live as described above from dd16 to dd23. Cyst areas were quantified using ImageJ, and statistically significant size changes were determined using paired t-test (each time point compared to dd16).

To assay the effects of compounds on late cyst growth when cysts had grown extensively and detached from the parent organoid, cysts where expanded and passaged through dissociation and reformation in low adherence cell plates. *PKD1*-/- and *PKD2*-/- cysts reaching  $\geq$  1mm in diameter were embedded in methylcellulose (day 0) and imaged at day 0 and day 3 using the Zeiss AxioZoom.V16 microscope. Growing cysts were treated with DMSO or QNZ (0.01, 0.1 and 1 µM) for 6 days, and were imaged every 3 days. Cyst areas were quantified using ImageJ, and statistically significant size changes were determined using ANOVA test.

#### Characterization of the organoid system

##### Single-cell RNA-seq data collection and analysis

Approximately 300 organoids were collected at dd8, dd10, dd14, dd16 and dd28 for scRNA-seq. The organoids were dissociated using 7.5 mg/ml *Bacillus licheniformis* cold active protease (Creative Enzymes, NATE-0633) mixed with 10 mg/ml collagenase type 2 (Worthington, #LS00417) and 125 U/ml DNase I (Worthington, #LS002058) in DPBS (150 µl) at 12°C for 20 min. The digestion mix was mixed twenty times with P-1000 wide-bore pipette tips. The dissociation reaction was terminated by mixing with 150 µl of 20% fetal bovine serum in DPBS. The cells were filtered through a pre-wetted 40-µm strainer (Falcon), and 1 ml of DPBS was used to wash cells off the strainer. The 1.3 ml of dissociated cell mix was combined with 3 ml of AutoMACS Running Buffer (Miltenyl Biotec, 130-091-221) and cells were briefly pelleted at 1250 rpm at 4°C. The cell pellet was then resuspended in 350 µl of AutoMACS Running Buffer, with 14 µM DAPI and 5 µM DRAQ5 added freshly. Single live cells (DAPI- and DRAQ5+) were selected by fluorescence-activated cell sorting (FACS) and single cell profiling with a 10x Genomics Chromium Single Cell 3' GEM, Library & Gel Bead Kit (10X Genomics, PN-1000075). After recovery from the emulsion, cDNA was cleaned-up and amplified by PCR, examined on a 4200 Tape station (Agilent) for yield assessment, and then processed into barcoded library for Illumina sequencing. Paired-end sequencing on the Illumina HiSeq 4000 platform was performed using the HiSeq 3000/4000 SBS PE clustering kit (PE-410-001) and 150 cycle flow cell (FC-410-1002). From fastq files, quality control, alignment to reference genome (hg38) and generation of count tables of the five libraries were done using CellRanger 3.1 (10X Genomics).

The Seurat 3.0 package was used for scRNA-seq analyses (Stuart et al., 2019). The five datasets were merged using the merge function. To filter out low-quality cells, we kept cells that had between 500 and 5,500 features, fewer than 20,000 RNA counts,

and less than 20% mitochondrial gene content. We integrated the datasets using the “Fast integration using reciprocal PCA” workflow presented by the Satija group ([https://satjalab.org/seurat/articles/integration\\_rpca.html](https://satjalab.org/seurat/articles/integration_rpca.html)). To summarize, the merged dataset was split into a list of two Seurat objects based on their origins: group 1 consisted of day 8, 10, 13 and 16, and group 2 composed of day 28 cells (the day 28 dataset was sequenced at a different sequencing depth from other timepoints). We then normalized and identified variable features for each dataset independently using *NormalizeData* and *FindVariableFeatures*. Features that were repeatedly variable across the two Seurat objects were selected for integration run PCA on each dataset using *SelectIntegrationFeatures*. The *FindIntegrationAnchors* function was used to identify the anchors, and these anchors were used to integrate the two Seurat objects using *IntegrateData* with reduction specified as “rpca”. The default assay was switched to “integrated” before the integrated dataset was scaled and centered using. The *RunPCA* function was applied to calculate principle components (PCs), and 40 PCs were used to determine neighbor cells and cluster assignment (using the *FindNeighbors* and *FindClusters* functions). The UMAP reduction was calculated using *RunUMAP* to determine UMAP embedding. Differentially expressed genes of each cluster were found using the *FindAllMarkers* function. Clusters 2, 4, 5, 6, 7, 11, 12, 19 and 22 were subset for nephrogenic lineage examination. Using similar integration procedure, the nephrogenic subset was integrated based on their origins (day 28 versus other timepoints) before standard workflow was applied to identify clusters. Further filtering against non-nephrogenic clusters was performed based on differentially expressed gene list to achieve a “clean” *in vitro* nephrogenic subset.

The *in vivo* datasets of human week 17 fetal kidney from our 2019 study (Tran et al., 2019) (GSE124472) were used for comparison with the scRNA-seq profiles of the *in vitro* derived nephrogenic cell subset. After the nephrogenic cells were subset from the week 17 datasets, the *in vitro* and *in vivo* nephrogenic cells were merged using the *merge* function. The merged dataset was first split based on *in vitro* or *in vivo* origin of the cells. The split Seurat objects were then integrated using the Fast integration with reciprocal PCA as described above. The default assay was switched to “integrated” before the integrated dataset was analyzed using the standard workflow (*ScaleData*, *RunPCA*, *RunUMAP*, *FindNeighbors*, and *FindClusters*) as described above. Cell embedding was presented as a UMAP reduction output (Becht et al., 2018). “RNA” was used as the default assay (*DefaultAssay* function), and the integrated dataset was re-normalized using *NormalizeData* before assaying gene expression levels.

Similarly, the interstitial cell populations were extracted from the week 17 human fetal kidney dataset and merged with the organoid dataset. The *in vitro* and *in vivo* interstitial cells were then integrated using “rpca” reduction.

To compare single-cell transcriptomes of our organoids with kidney organoids generated by other groups, we retrieved published scRNA-seq datasets from various research groups (Combes et al., 2019; Czerniecki et al., 2018; Kumar et al., 2019; Subramanian et al., 2019; Tran et al., 2019; Wu et al., 2018) (listed in the *key resources table*). From each dataset, we extracted cells that had between 500 and 5,500 features, fewer than 20,000 RNA counts, and less than 20% mitochondrial gene content, and performed the standard Seurat workflow to find clusters, and annotated the clusters using the differentially expressed genes (identified using the *FindAllMarkers* function). Nephrogenic cells were further subset based on the annotations. The subset was subjected to the standard workflow to identify cell clusters, and the procedure would be repeated if non-nephrogenic cell groups were detected to further refine the nephrogenic cell extraction. The “clean” nephrogenic subsets from all datasets were merged with the human fetal kidney nephrogenic lineage subset, and then split based on their origins before being integrated using the fast integration with reciprocal PCA workflow as detailed above. The “integrated” default assay was selected before *ScaleData*, *RunPCA*, *RunUMAP*, *FindNeighbors*, and *FindClusters* were used to cluster cells (presented in Figures 3E–3H). The default assay was then switched to “RNA” before gene expression levels were assayed (presented in Figures 3F and S3A–S3C).

To compare the transcriptomic profiles of *in vitro* and *in vivo* nephron segment cells, the following clusters were extracted from the integrated *in vivo/in vitro* nephrogenic cell dataset: clusters 0 and 1 for podocyte, cluster 3 for proximal tubule, and clusters 9 and 13 for putative medial/distal nephron precursor. Each subset was merged, and clusters were identified. “RNA” was used as the default assay (*DefaultAssay* function), and the integrated datasets were re-normalized using *NormalizeData* before examination of gene expression levels. Differential gene test was performed using *FindAllMarkers* to look for genes highly expressed in the *in vitro* or the *in vivo* cells. To account for batch differences, these gene lists were compared with differentially expressed gene list from comparing the *in vitro* and *in vivo* interstitial cells, and genes that were present in all four lists (interstitium, podocyte, proximal tubule, and medial/distal nephron precursor) were considered “background differences”. Cell-type specific differences were presented in **Table S1**. Expression patterns and levels of representative differentially expressed genes were examined in the all-group comparison using feature plots with UMAP reduction with three subsets presented separately based on their origins (Figures S3A–S3C).

### Histology

Organoids were fixed in 4% paraformaldehyde for 10 minutes at 4°C temperature and were washed three times in 1XPBS. Samples were then transferred to an embedding mold with 15% sucrose/7.5% gelatin in PBS and incubated in the gelatin solution at 37°C until the organoids sink. The organoids in gelatin solution was then frozen in a dry ice/ethanol slurry. Samples were stored at -80°C until cryosectioning and processing.

### Immunohistochemistry and *in situ* hybridization

Frozen sections were warmed to room temperature for 10 minutes before the staining procedure. Citrate Buffer pH 6.0 (Sigma) was used for antigen retrieval in a pressure cooker. The slides were then washed with water and air dried for 5 min. 1.5% Seablock (ThermoFisher) in PBS + 0.25% TritonX block buffer was applied on the tissue for 1 hour at room temperature for blocking. The slides were then incubated with primary antibody mixture (diluted in block buffer) at 4°C overnight. Primary antibodies used in the study are listed as follow: WT1 (abcam, ab89901, 1:5000), JAG1 (R&D, AF599, 1:300), LAMB1 (Santa Cruz, sc-33709, 1:50), SOX9 (abcam, ab185230, 1:1000), HNF4A (R&D, MAB4605, 1:500), CUBN (R&D, AF3700, 1:500), SLC12A1 (Sigma, HPA018107, 1:500), LTL (Vector

Laboratories, FL-1321, 1:300), SLC3A1 (Sigma, HPA038360, 1:500), NPHS1 (abcam, ab136927, 1:5000), POU3F3 (ThermoFisher, PA5-64311, 1:500), MAFB (R&D, MAB3810, 1:500), PAX8 (abcam, ab189249, 1:1000), CDH1(Biosciences, 610182, 1:300), PAX2 (R&D, AF3364, 1:500), GATA3 (R&D, AF2605, 1:300), ACE2 (R&D, AF933, 1:500). Secondary antibodies conjugated with AlexaFluor 488, 555, 594, and 647 (diluted to 1:1000 in block buffer) purchased from Molecular Probes. To stain the nuclei, slides were treated with 1 mg/ml Hoechst 33342 (Molecular Probes) in PBS for 5 min. ProLong Gold Antifade Reagent (Life technologies) was applied on the tissue for mounting, and images were acquired at 40X using the Leica SP8 confocal microscope.

#### **RNA extraction, cDNA synthesis and quantitative polymerase chain reaction**

About 200 organoids were collected for transcriptional analyses for each time point. The RNeasy Micro Kit (Qiagen, 74004) was used for RNA extraction following the manufacturer's protocol. cDNA was synthesized from 200 µg of RNA for each sample using the SuperScript IV VILO Master Mix with ezDNase enzyme (Invitrogen, 11766050).

Quantitative polymerase chain reaction (qPCR) was performed using the Taqman Fast Advanced Master Mix (ThermoFisher, 444557) following the manufacturer's instruction on the ViiA 7 Real-Time PCR System (ThermoFisher). The following probes from ThermoFisher were used for transcriptional analyses: *WT1* (Hs01103751\_m1), *MAFB* (Hs00534343\_s1), *PAX2* (Hs01057416\_m1), *HNF4A* (Hs00230853\_m1), *GATA3* (Hs00231122\_m1), *SLC3A1* (Hs00942976\_m1), *SLC12A1* (Hs00165731\_m1) and *SLC12A3* (Hs01027568\_m1).

#### **Western Blot**

To prepare protein lysate samples, organoids and control samples were suspended and homogenized in lysis buffer (RIPA buffer (Pierce, 89901) supplemented with 1 mM benzamidine hydrochloride (TCI America, TCB0013), 1X protease inhibitor cocktail (Cell signaling, 5871), 100 µM PMSF (Sigma-Aldrich, 11359061001), and protease inhibitor cocktail tablets (one tablet/10ml of buffer) (Sigma, 11836170001)), and left on ice for 30mins. Next, samples were centrifuged for 15 min at 16,000×*g* at 4°C, and supernatants were transferred to low protein binding tubes (Eppendorf). Total protein concentrations were measured using the BCA protein assay kit (Pierce, 87003-294), according to manufacturer's instructions. Protein lysates were flash frozen and stored at -80°C.

Protein lysates were separated by SDS-polyacrylamide gel electrophoresis (SDS-PAGE). 4–15% Mini-PROTEAN™ TGX Stain-Free™ Protein Gels (Bio-Rad, 4568086) were used. After electrophoresis, protein lysates were electroblotted to methanol activated Low-Fluorescence PVDF Transfer Membranes (Bio-Rad, IPFL20200). Membranes were then dried at 37°C for 5 minutes and then re-activated with methanol. Blots were stained with Li-Cor's Revert-700 Total Protein Stain (Li-Cor, 926-11010) for normalization and imaged using a Li-Cor Odyssey Clx. In the subsequent incubation and washing steps, blots were placed on an orbital shaker. Blots were then de-stained following the manufacturer' instruction and were incubated in block buffer (Li-Cor Intercept block, 13 927-60001) for 1 hour at room temperature. Blots were then transferred to a primary antibody mix (in block buffer supplemented with 0.1% Tween20) and were incubated overnight at 4°C. The following primary antibodies were used: PKD1 (Kerafast, Clone E8-8C3C10, catalog number EMD303) (Yu et al., 2007), PKD2 (Santa Cruz, sc-28331). On the following day, blots were washed four times in TBS-T (5 min each) at room temperature, and then incubated in secondary antibody (1:10,000) in block buffer with 0.1% Tween20 and 0.1% SDS for 1 hour at room temperature. The following secondary antibodies were used: IRDye® 800CW Goat anti-Rat IgG (H + L) (Li-Cor, 926-32219) for PKD1; IRDye® 680RD Donkey anti-Mouse IgG (H + L) (Li-Cor, 926-68072) for PKD2. Blots were then washed twice with TBS-T for 5 minutes each at room temperature, followed by two 5-minute TBS washes at room temperature. Blots were imaged using the Li-Cor Odyssey Clx system.

#### **mRNA-Seq and data analysis**

Samples were prepared according to library kit manufacturer's protocol (Clontech SMARTer), indexed, pooled, and sequenced on an Illumina NovoSeq 6000. Basecalls and demultiplexing were performed with Illumina's bcl2fastq software and a custom python de-multiplexing program with a maximum of one mismatch in the indexing read. RNA-seq reads were then aligned to the Ensembl release 76 primary assembly with STAR version 2.5.1a (Dobin et al., 2013). Gene counts were derived from the number of uniquely aligned unambiguous reads by Subread:featureCount version 1.4.6-p5 (Liao et al., 2014). logCPM values were obtained with the 'EdgeR' package (Robinson et al., 2010) and used to calculate the pairwise correlation coefficients between samples. TPM values were calculated based on CPM and length of exon models of genes in the corresponding annotation. Differential expression analysis was performed with DESeq2 (Love et al., 2014), with thresholds described in supplementary tables. To generate the heatmaps in Figures S7C–S7F, top 50 differentially expressed genes by adjusted p-values were extracted and ranked by fold change; for each gene, the log<sub>2</sub>-transformed TPM in each sample was normalized by the mean value across all samples in comparison before plotting with 'heatmap.2' function in the 'gplots' package in R. Gene Ontology (GO) analysis was performed with the 'clusterProfiler' package in R (Yu et al., 2012), with only top 3 terms by p-value shown. For a full list of TPM values of all samples, please refer to Table S1.

#### **TUNEL assay**

Cryo-sections were stained with the Click-iT Plus TUNEL Assay kit (Invitrogen) by following the manufacturer's instruction. Briefly, the sections were incubated with the TdT reaction buffer for 10 min at 37°C. The slides were then rinsed with deionized water and incubated with 3%BSA and 0.1% Triton X-100 in PBS for 5 minutes followed by PBS washing. Next, the samples were incubated with the Click-iT Plus TUNEL reaction cocktail in a humidified chamber at 37 °C for 30 min protected from light. This was followed by PBS washes and incubation with 2% sea block for 1hrs. After that, we performed immunofluorescent staining as detailed above.

#### **FACS analysis**

Upon dissociation using 7.5 mg/ml *Bacillus licheniformis* cold active protease (Creative Enzymes, NATE-0633) mixed with 10 mg/ml collagenase type 2 (Worthington, #LS00417) and 125 U/ml DNase I (Worthington, #LS002058) in DPBS (150 µl) at 12°C for 20 min,

organoid cells were pelleted. The pellet was resuspended in autoMACs running buffer containing DAPI (1:1000) and DRAQ5 (1:2000) then analyzed on an ARIA II FACS using gates to detect DRAQ5+ and DAPI- cells.

### Vascularization of transplanted kidney organoids

#### *Renal capsule transplant*

All surgical procedures were carried out with appropriate oversight and compliance following guidelines after institutional review by USC's Institutional Animal Care and Use Committee (IACUC). The procedure was adapted from (Yoshimura et al., 2017). Week 8–12 NOD.CB17-Prkdc<SCID>/J mice were anesthetized with Ketamine/Xylazine. The surgery site on the dorsal flank was shaved and swabbed with Proiodine/alcohol. An 8–10 mm incision was made in the flank and the fascia was incised before the kidney was exteriorized. The kidney capsule was kept moist with sterile saline during the procedure. A small incision was made in the outer membrane of the renal capsule at the caudal end, using a sharp 24g needle and the sub capsular space is flushed with 1ml of basal differentiation media using a blunted 24g needle 30g needle (B30-50, Strategic Applications, Inc.) attached to a 1 ml syringe. Two agarose rods (2mm long, 0.5mm diameter) were pushed into the sub capsular space in the shape of an open V using forceps. A 20g indwelling needle (SURFLO® PTFE I.V. Catheter needle, VWR, TESR-OX2025CA) attached to a 1 ml syringe and draw up 3–4 dd13–14 organoids basal differentiation media into the needle. The indwelling needle was inserted under the renal capsule to place organoids between the agarose rods. The capsule incision was cauterized, and the kidney was replaced into the retroperitoneum. The muscle layer was sutured, and the skin was closed with wound clips.

#### *In vivo dextran uptake assay*

Two weeks after the implantation of kidney organoids, NOD/SCID mice were anesthetized with isoflurane (3% in induction chamber). 200 µl of fluorescently labelled dextran (3 and 70 kDa) diluted in PBS or sterile PBS (negative control) was administered by retro-orbital injections. 10 minutes after the injection, the mice were euthanized, and the kidneys were collected. The mixture of fluorescent dextran was consisted of 100 µl Tetramethylrhodamine-conjugated 70 kDa lysine fixable dextran (Invitrogen, D1818) (1 mg/animal) and 100 µl of 3000 Da MW Texas Red™ conjugated dextran (Invitrogen, D3328) (1 mg/animal). We chose the 3 kDa dextran as the low molecular weight and the 70 kDa dextran as the high molecular weight dextran in the physiologically relevant ranges to investigate the glomerular filtration barrier based on previous studies by van den Berg et al. (2020). To label the proximal tubules on the cryosections of the dextran-injected kidneys, immunofluorescence was performed using LRP2 antibody (MyBioSource, MBS690201). All animal protocols were approved by the Institutional Animal Care and Use of Committee at the University of Southern California.

#### *Image acquisition and analysis*

Image acquisition of sections was performed using Leica SP8-X confocal fluorescence imaging system (Leica Microsystems, Germany) in 1024×1024 pixels using a 63X Leica oil immersion objective (NA 1.6). Image masking was performed and quantified with Imaris 9.7 software (Oxford Instruments, United Kingdom). The thresholding of the signal of 3000 Da dextran was based on the intensity histogram of Texas Red™. Fluorescent punctae larger than 1.25 µm<sup>2</sup> were scored. Masks were classified to their respective anatomical structures based on the presence of LRP2/MAFB markers.

## QUANTIFICATION AND STATISTICAL ANALYSIS

Details of sample size were provided in the [method details](#) section for each experiment. Wilcoxon Rank Sum test was performed, and p-values were presented in [Figure 5D](#). Kruskal-Wallis test was performed, and p-values were presented in [Figures S6D–S6I](#). Paired t-test was performed, and p-values were summarized in [Figure 7C](#). ANOVA test was performed for [Figures 7D, S7B, S7I](#), and [S7L](#).

**Supplemental Information**

**A scalable organoid model of human autosomal dominant polycystic kidney disease for disease mechanism and drug discovery**

**Tracy Tran, Cheng Jack Song, Trang Nguyen, Shun-Yang Cheng, Jill A. McMahon, Rui Yang, Qiuyu Guo, Balint Der, Nils O. Lindström, Daniel C.-H. Lin, and Andrew P. McMahon**

## SUPPLEMENTAL FIGURE LEGENDS

### **Figure S1: Immunofluorescent and qPCR analyses of human fetal kidney and organoids (related to Figure 1)**

- (A) Immunofluorescent analyses of the human week 15-17 fetal kidney cryosections as positive controls for these analyses on the organoids. Scale bars indicate 50 µm.
- (B & C) Immunofluorescent analyses of the day13 and day14 organoids indicating the emergence of cells resembling human nephron segments. Scale bars indicate 50 µm.
- (D) Immunofluorescent analyses of the day22 and day28 organoids indicating the presence of cells resembling human nephron segments. Scale bars indicate 50 µm.
- (E) qPCR analyses showing upregulation of nephron markers along the differentiation timeline in organoids derived from MAFB-P2A-eGFP H9 hESC.
- (F) qPCR analyses comparing expression levels *MAFB*, *HNF4A*, *GATA3*, *ANXA1*, *SLC3A1* and *SLC12A1* expression between Day16 and Day 28 groups of individual organoids.
- (G) Immunofluorescent analyses of the day16 and day28 organoids derived from Kolf2.1J iPSCs indicating the presence of cells resembling human nephron segments. Scale bars indicate 50 µm.
- (H and I) qPCR analyses showing upregulation of nephron markers along the differentiation timeline in organoids derived from the Kolf2.1J iPSC line.

### **Figure S2: scRNA-seq analyses of organoids (related to Figure 2)**

- (A) UMAP reduction of cell clusters in organoids colored by clusters and hierarchical clustering of cell identities in organoids.
- (B) Dotplot of gene markers used for identification of cell clusters in organoids.
- (C) UMAP reduction of cell clusters in organoids colored by original identities.
- (D) Bar graph of cell count presenting contribution of different original identities to the cell clusters in organoids.
- (E) Feature plots of transcription factor genes on UMAP reduction of the nephrogenic lineage in organoids.
- (F) UMAP reduction of cell clusters in day 28 organoids from 2 batches of differentiation colored by their original identities.
- (G) Bar graph of cell count presenting contribution of different original identities to the cell clusters in day 28 organoids from 2 batches.
- (H) UMAP reduction of cell clusters in day 28 organoids from 2 batches of differentiation colored by clusters.
- (I) Dotplot of gene markers used for identification of cell clusters in day 28 organoids from 2 batches.

### **Figure S3: scRNA-seq analyses of organoids (related to Figure 3)**

(A-C) Feature plots of genes differentially expressed between *in vitro* and *in vivo* kidney cells using UMAP reduction of cells extracted by their origins.

(D) UMAP reduction of interstitial cell clusters in organoids colored by clusters.

(E) Dotplot of gene markers used for identification of interstitial cell clusters in organoids.

(F) UMAP reduction of interstitial cell clusters from human fetal kidney and organoids, colored by clusters.

(G) UMAP reduction of interstitial cell clusters from human fetal kidney and organoids, colored by their original identities.

(H) Dotplot of gene markers used for identification of interstitial cell clusters from human fetal kidney and organoids.

(I) Bar graph of cell count presenting contribution of different original identities to the of interstitial cell clusters from human fetal kidney and organoids.

#### **Figure S4: Vascularization of organoids (related to Figure 4)**

(A-E) Immunofluorescent analyses of cryosectioned vascularized MAFB-P2A-eGFP organoids. Scale bars indicate 50 µm.

(F) Immunofluorescent analyses of cryosectioned vascularized MAFB-P2A-eGFP organoids collected 10 minutes post dye injection. Scale bars indicate 50 µm.

(G) Pie chart showing proportions of fluorescent signal areas in three categories: LRP2+, MAFB+, and non-tubular/undetermined cells.

#### **Figure S5: Validation of PKD mutant lines, qPCR and immunofluorescent analyses of PKD mutant organoids (related to Figure 5)**

(A and B) Sanger sequencing reads of PCR clones amplified from the *PKD1*-/- mutant to validate the location of indel mutations on the real gene loci.

(C-E) Western blots validating the expression or loss of protein expression of PKD1 and PKD2 in controls and PKD mutant lines. Arrowhead: Full-length PKD1. Arrow: cleaved PKD1

(F-H) qPCR analyses showing upregulation of nephron markers along the differentiation timeline in organoids derived from (F) *PKD2*-/- H9 hESC, (G) 5-T hESC, and (H) 5-T *PKD1*-/- hESC.

(I and J) Brightfield images and quantification of identifiable cyst formation rates of *PKD2*-/- organoids started at different cell number. Scale bars indicate 200 µm.

(K) Large *PKD2*-/- cysts after 3 months in culture. Scale bar indicates 1 mm.

(L) Immunofluorescent analyses showing contribution of different nephron segment-like cells to cystic epithelial cells. Scale bars indicate 50 µm.

(M) Immunofluorescent analyses of the day28 organoids and cysts from PKD mutant lines showing cell polarity and cilia protrusion. Scale bars indicate 50 µm.

**Figure S6: Effects of drug treatments on PKD mutant cyst formation (related to Figure 6)**

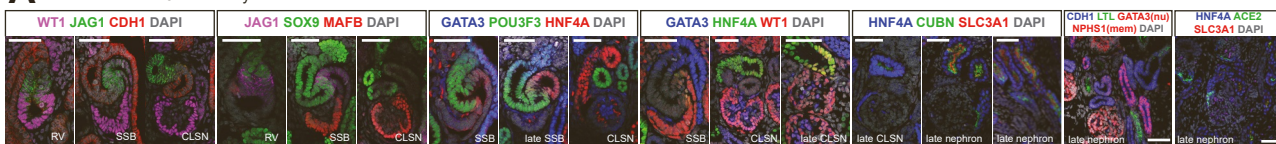
- (A) Z-scores calculations based on cyst formation rates of DMSO-treated *PKD1*-/- or *PKD2*-/- mutants.
- (B) Brightfield images showing examples of “non-hit”, “true hit” or “non-specific” growth inhibitor compounds. Red asterisks indicate organoids showed at higher magnification. Red arrowheads indicate identifiable cysts. Scale bars indicate 500 µm.
- (C to H) Boxplots showing cyst formation rates of *PKD1*-/- or *PKD2*-/- mutants treated with either DMSO or different concentrations of Blebbistatin, 8-Br-cAMP or Forskolin.

**Figure S7: Effects of QNZ on organoid/cyst formation and progression (related to Figure 7)**

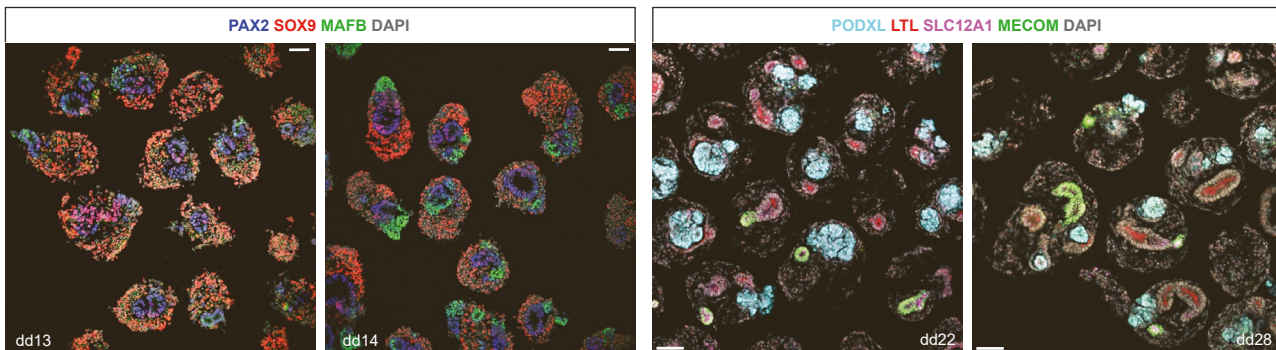
- (A) Effects of low QNZ concentrations on *PKD1*-/- late cysts compared to DMSO (monitored from day 0 to day 9; QNZ administered on day 3) (Data are represented as mean ± SEM). Scale bars indicate 500 µm.
- (B) Brightfield and fluorescent images showing podocyte-like cells emergence when MAFB-eGFP organoids were treated with various concentrations of QNZ (monitored from dd16 – dd23). Scale bars indicate 500 µm.
- (C) Quantification of MAFB-eGFP organoids’ areas from images presented in panel B (Data are represented as mean ± SEM).
- (D) qPCR analyses examining relative expression levels of *MAFB*, *SLC3A1*, *SLC12A1*, and *GATA3* in MAFB-eGFP organoids treated with various concentrations of QNZ compared to DMSO treated ones.
- (E-G) Heatmaps showing differentially expressed genes and their Gene Ontology terms from various RNA-seq analyses comparing QNZ-treated with DMSO-treated organoids or cysts. (extended list of GO terms in Supplemental Table 1).
- (H) Immunofluorescent analyses showing apoptotic cells in *PKD2*-/- organoids treated with DMSO, QNZ 20 nM, QNZ 10 µM, and Staurosporine 0.1 µM from dd14 to dd20. Samples were collected at dd20 for analyses. Scale bars indicate 500 µm.
- (I) Percentage of TUNEL+ cells among PODXL+ podocytes (PODs), PODXL- cell types (CTs), CUBN+ proximal tubule (PT) cells, and CUBN- cell types (CTs) based on figure S7H (Data are represented as mean ± SEM).
- (J) Percentage of DRAQ5+ DAPI- live cells (measured by FACS) in cells dissociated from *PKD1*-/- or *PKD2*-/- organoids treated with DMSO, various concentrations of QNZ, and 0.1 µM Staurosporine.
- (K) Immunofluorescent analyses showing apoptotic cells in *PKD1*-/- or *PKD2*-/-*PKD2*-/- cysts treated with DMSO, 0.01 µM QNZ, 1 µM QNZ, or 0.1 µM Staurosporine for 3 days.
- (L) Percentage of TUNEL+ cells among ZO1+ cells in cysts based on Figure S7K (Data are represented as mean ± SEM).

# Figure S1

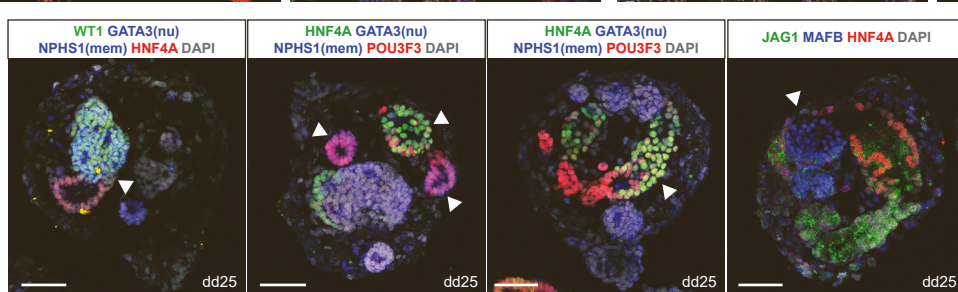
**A** Human Week 15-17 Kidney



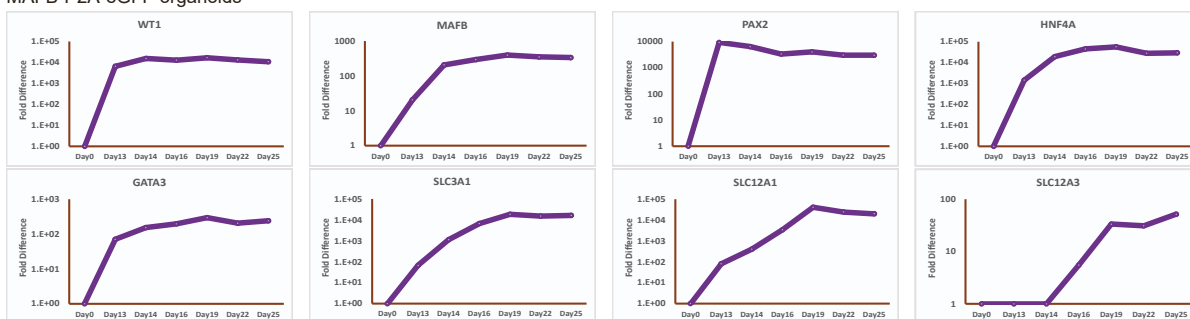
**B**



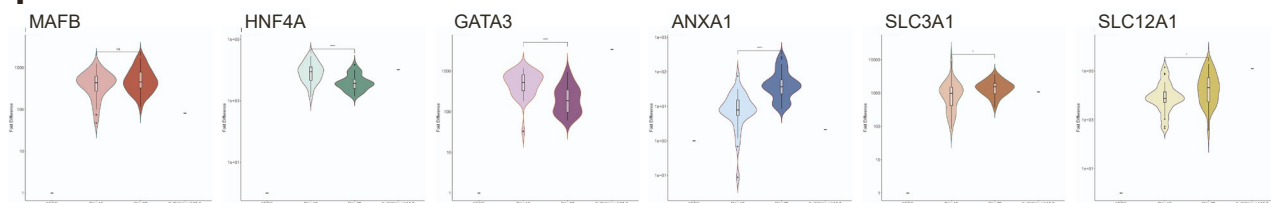
**D**



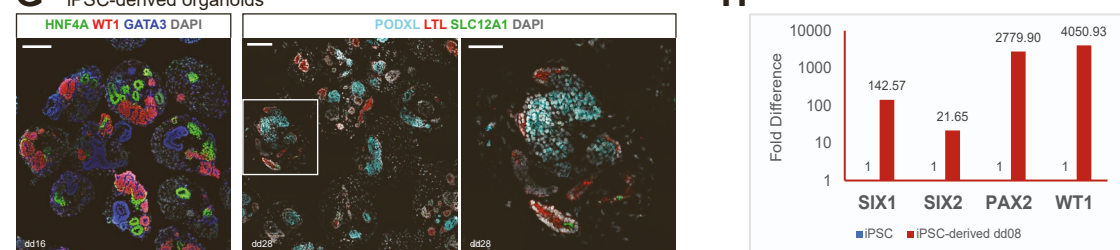
**E** MAFB-P2A-eGFP organoids



**F**



**G** iPSC-derived organoids



**I** iPSC-derived organoids

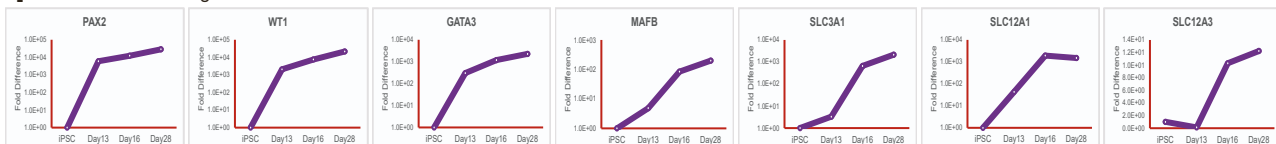


# Figure S2

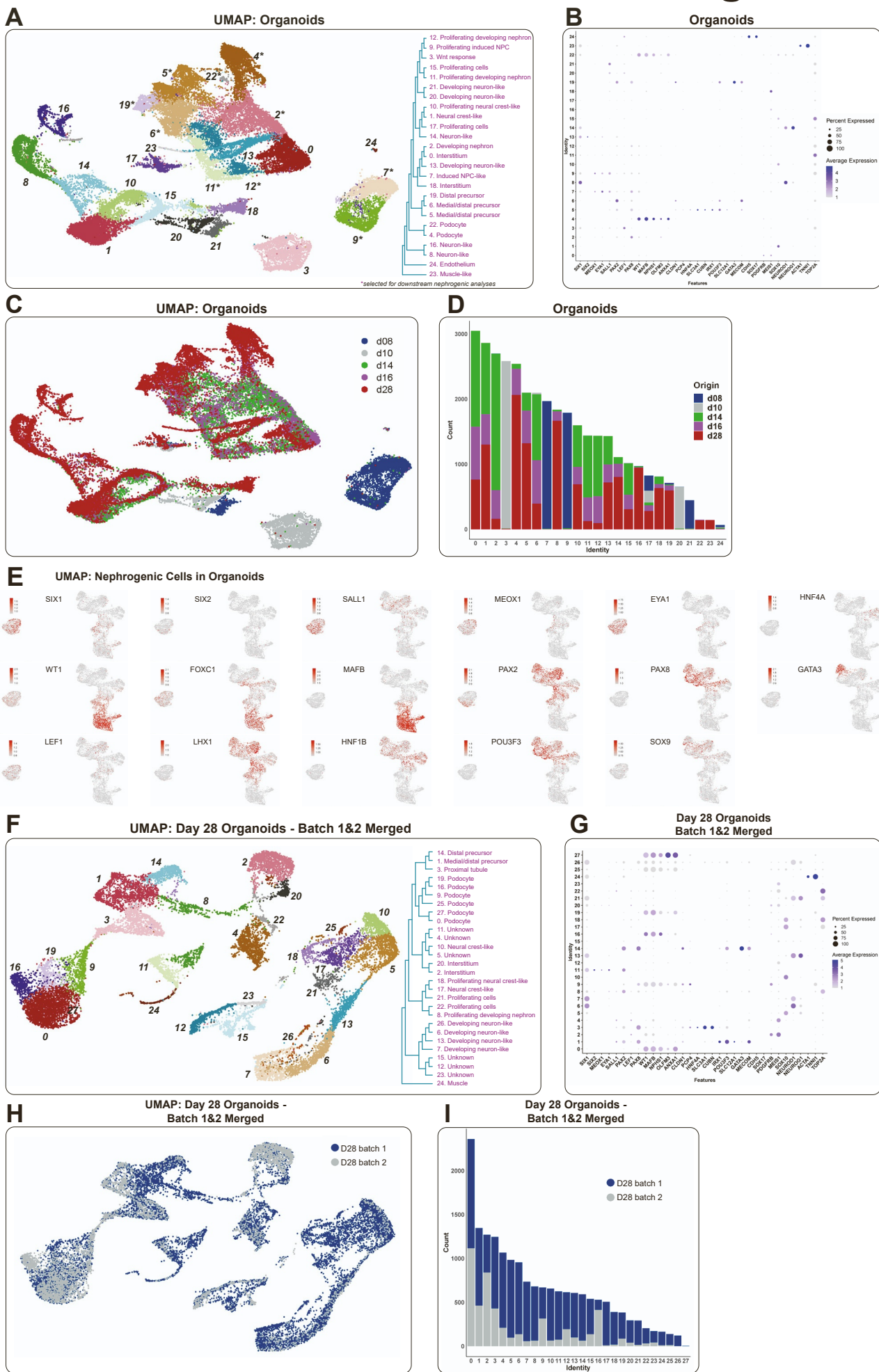
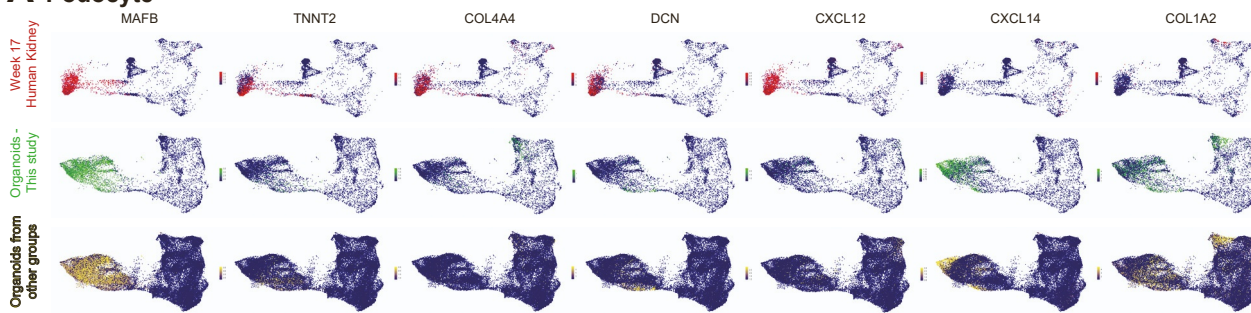
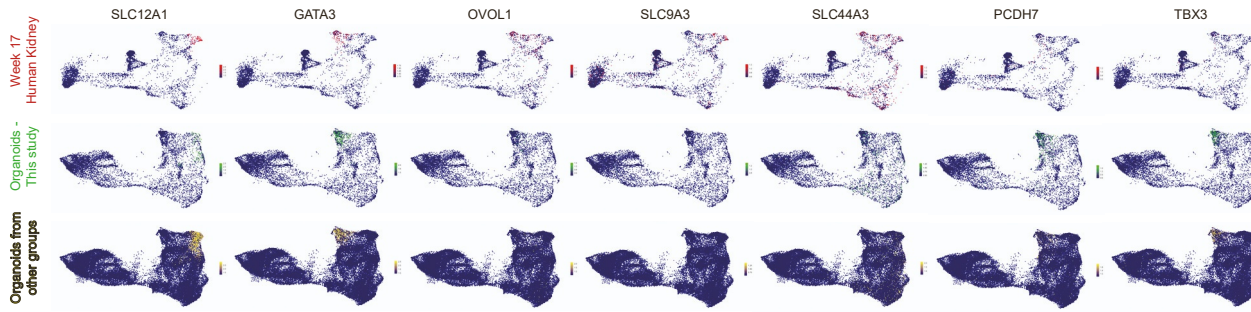


# Figure S3

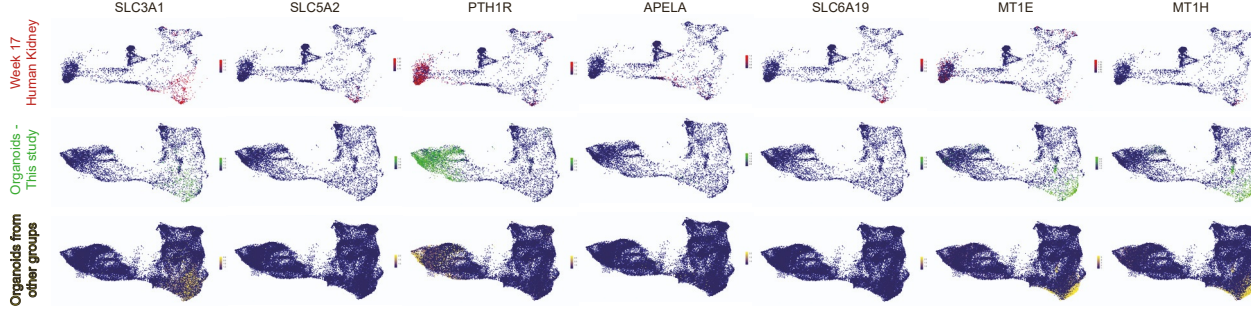
## A Podocyte



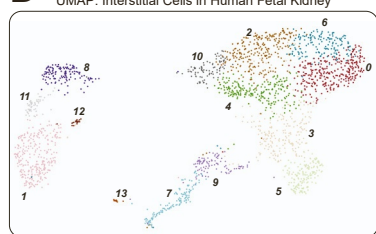
## B Medial/Distal Precursor



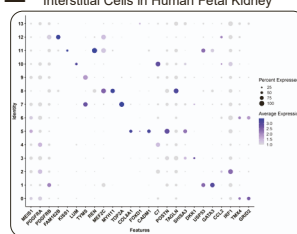
## C Proximal Tubule



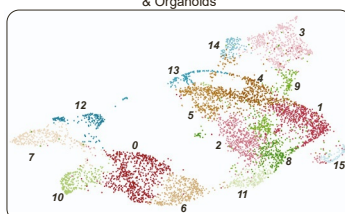
## D UMAP: Interstitial Cells in Human Fetal Kidney



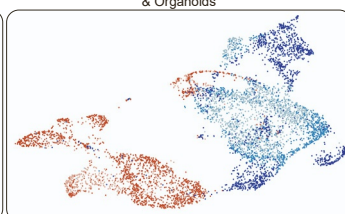
## E Interstitial Cells in Human Fetal Kidney



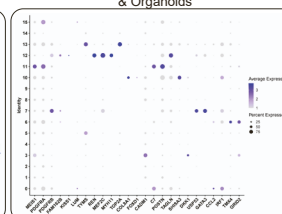
## F UMAP: Interstitial Cells in Human Fetal Kidney & Organoids



## G UMAP: Interstitial Cells in Human Fetal Kidney & Organoids



## H Interstitial Cells in Human Fetal Kidney & Organoids



## I Interstitial Cells in Human Fetal Kidney & Organoids

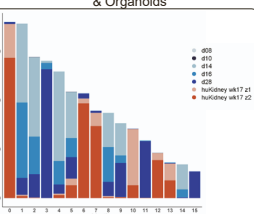


# Figure S4

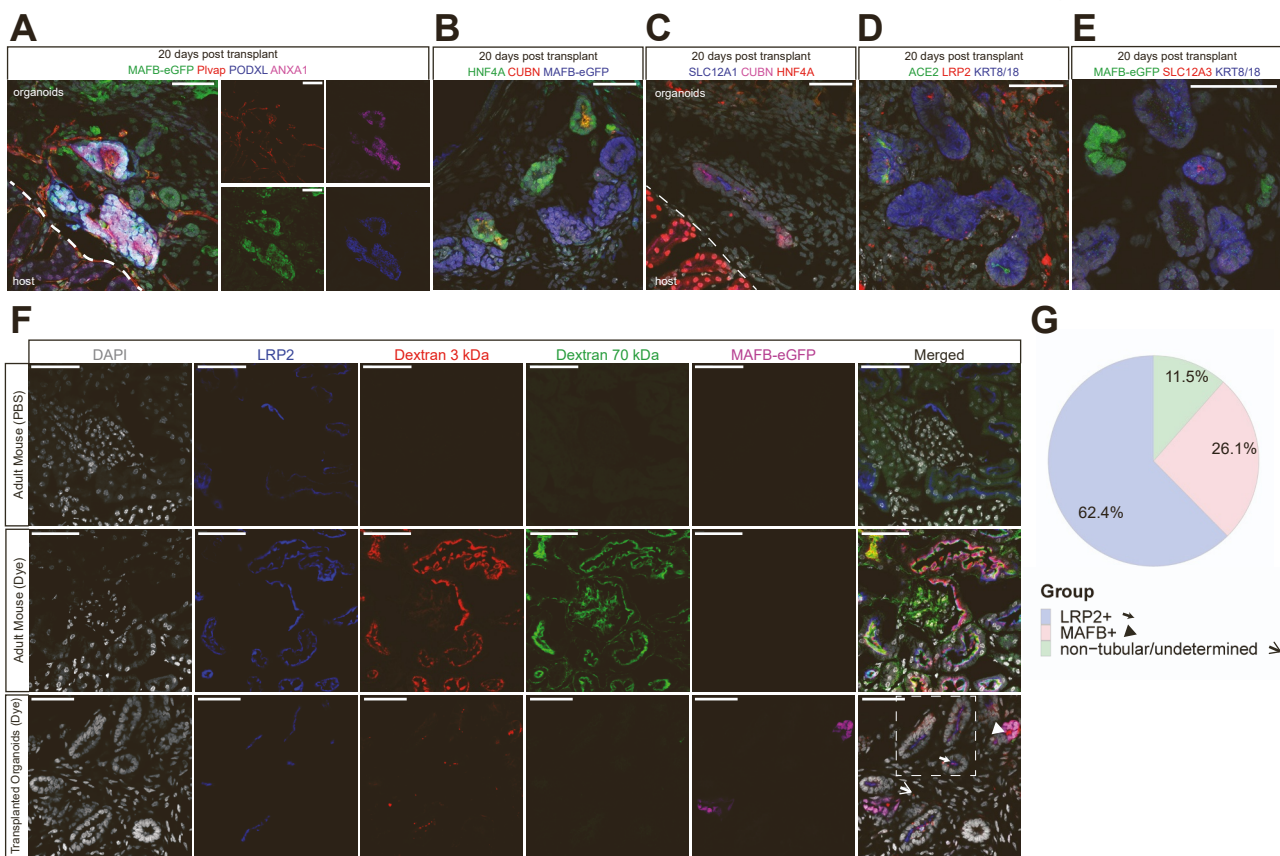


# Figure S5

**A**

Sequence name	Location	Sequencing Read
<i>PKD1</i> ref seq. (NC_000016.10)	91	TCTGCCCTCGGACACGGAGATCTTCCCCTGGCAACCGGCACGTGCTACC
Mutant (clones no. 1-5)	285	TCTGCCCTCGGACACGGAGATCTTCCCCT-GCAACGGGCACGTGCTACC
Pseudogene (clones no. 6-11)	337	TCTGCCCTCGGACACGGAGATCTTCTGGCAACGGGCACGTGCTACC
Pseudogene (clones no. 12-35)	285	TCTGCCCTCGGACACGGAGATCTTCTGGCAATGGGCACGTGCTACC
Mutant (clones no. 36-38)	318	TCTGCCCTCGGA-----ACGGGCACGTGCTACC

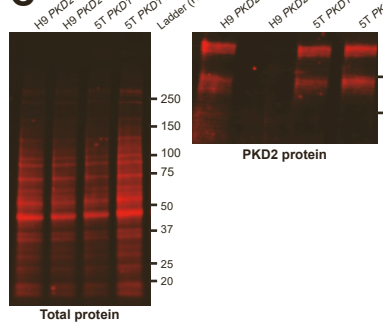
■ PAM seq. ■ gRNA ■ gene/pseudogene variants ■ indel mutations

**B**

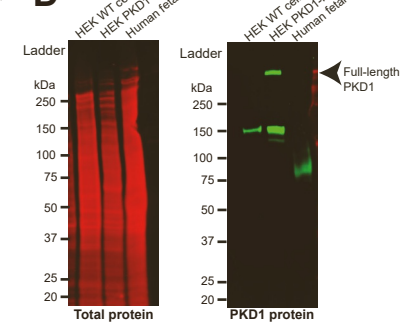
Sequence name	Location	Sequencing Read
<i>PKD2</i> ref seq. (NC_000004.12)	28570	TCTTTCTGTGTTCCAGTGCACCTACGGCATGATGAGCTCAAATGTGACTACTACACCCC
Mutant (clones no. 1-22)	302	TCTTTCTGTGTTCCAGTGCACCTACGGCATGATGAGCTCAAATGTGACTACTACACCCG
Mutant (clones no. 23-42)	183	TCTTTCTGTGTTCCAGTGCACCTACGGCATGATGAGCT-----A-C-----TGATGTCACAGCTTCTTAGACACCCCC

■ PAM seq. ■ gRNA ■ indel mutations

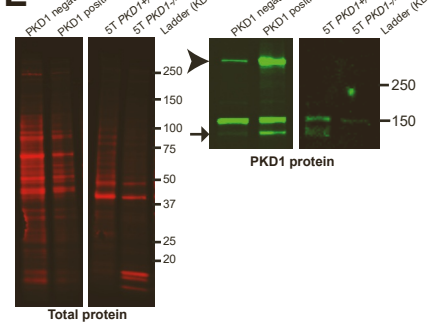
**C**



**D**



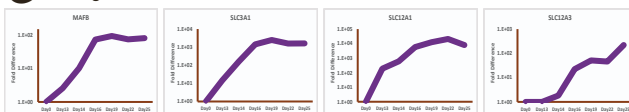
**E**



**F PKD2-/- organoids**



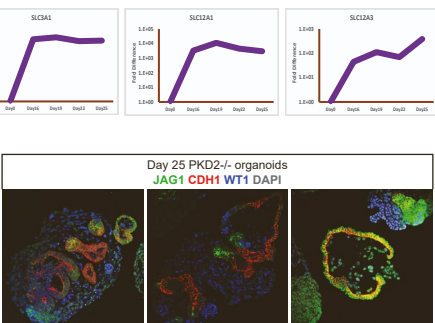
**G 5-T organoids**



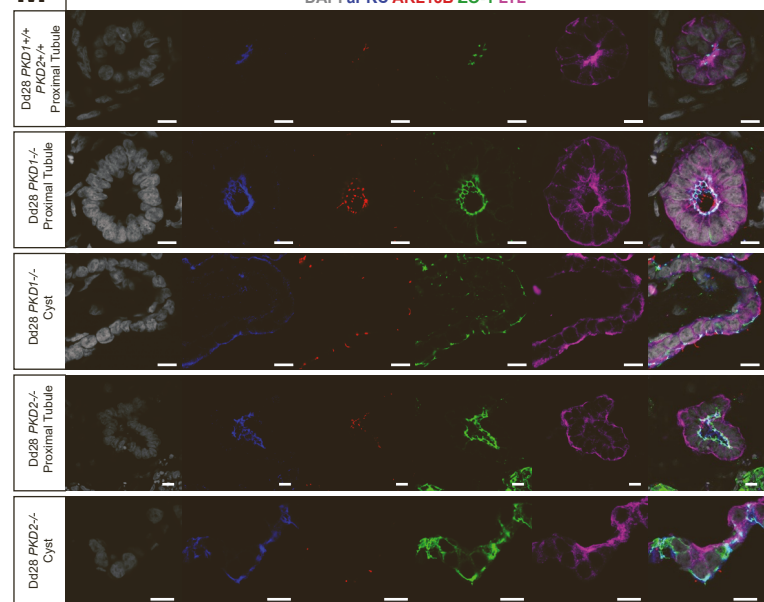
**K**



**H 5-T PKD1-/- organoids**



**M**



**J**

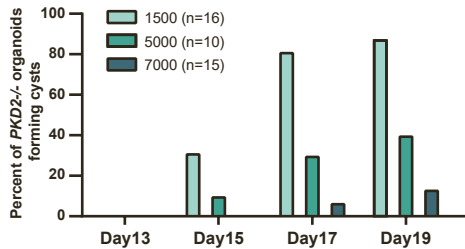
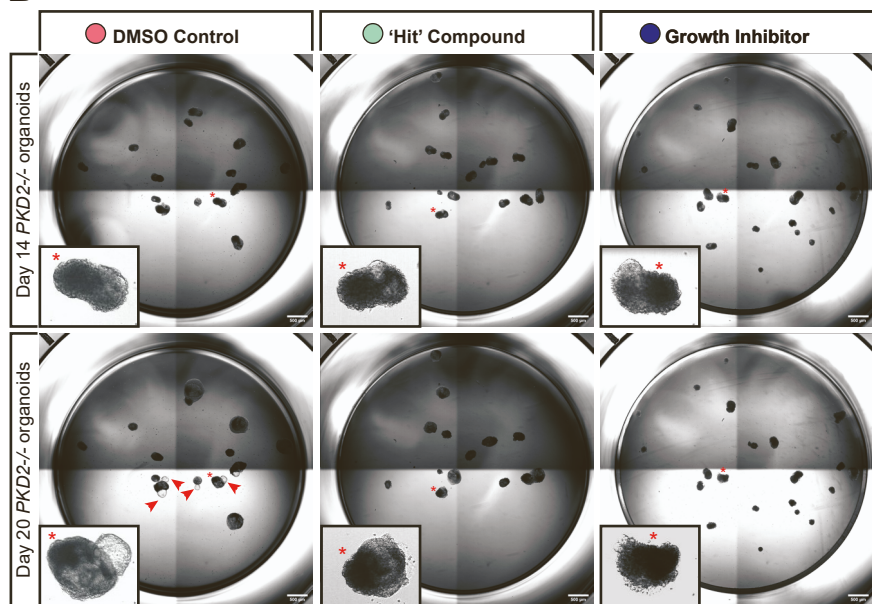


# Figure S6

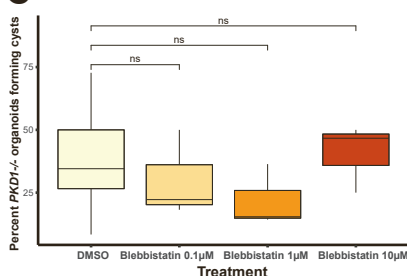
**A**

	Day15	Day16	Day17	Day18	Day19	Day20
<i>PKD1</i> -/-	-1.07	-0.65	0.07	0.27	0.40	0.40
<i>PKD2</i> -/-	-5.74	-1.60	-0.03	0.22	0.37	0.37

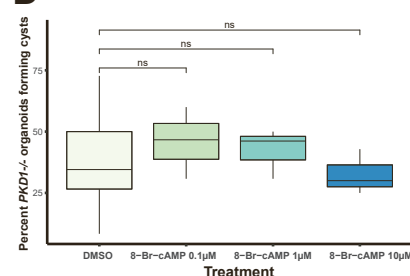
**B**



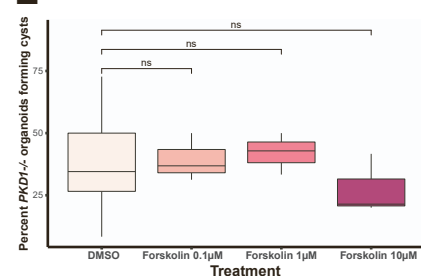
**C**



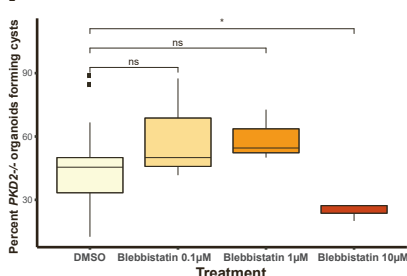
**D**



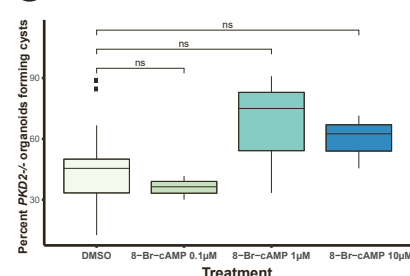
**E**



**F**



**G**



**H**

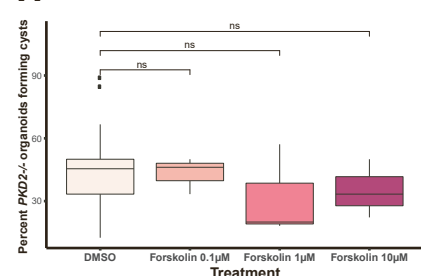


# Figure S7

